# Detailed Spectral Studies of Copper Acetate: Excited-State Interactions in Copper Dimers

**Paul K. Ross, Mark D. Allendorf, and Edward I. Solomon***

*Contribution from the Department of Chemistry, Stanford University, Stanford, California 94305.* *Received September 29, 1988*

**Abstract:** A combination of linearly polarized absorption, transverse and longitudinal Zeeman, and variable-temperature magnetic circular dichroism spectroscopies have been used to assign 10 ligand field excited states of copper acetate pyrazine and measure the splittings between these states. Due to interactions between coppers, each monomer d-d transition splits into four in the dimer: g and u combinations of singlets and triplets. This splitting is governed by three terms: the excited-state exchange interaction ($J_{n,x^2-y^2}$) and the Coulomb ($I_{n,x^2-y^2}$) and exchange ($L_{n,x^2-y^2}$) contribution to excitation transfer between metal centers. The value of $L_{n,x^2-y^2}$ is further related to $J_{n,n}$, the exchange interaction between half-occupied $d_n$ orbitals on each copper. The experimental measurement of $J_{n,x^2-y^2}$ and $L_{n,x^2-y^2}$ has allowed evaluation of the exchange interactions between all combinations of electrons in the different $d_n$ orbitals in the copper acetate structure. For the orthogonal pathway, $J_{n,x^2-y^2}$, we find $-2J_{xy,x^2-y^2} > 0 > -2J_{xzyz,x^2-y^2} > -2J_{z^2,x^2-y^2}$ with $-2J_{xy,x^2-y^2}$ being weakly antiferromagnetic, while for the nonorthogonal $J_{n,n}$ pathway the order is $-2J_{xzyz,xzyz} > -2J_{x^2-y^2,x^2-y^2} > -2J_{xy,xy} > -2J_{z^2,z^2}$. In addition, the $^3A_{1u}$ component of the $d_{x^2-y^2} \leftarrow d_{xy}$ excited state exhibits sharp vibronic structure which was perturbed in Zeeman experiments. The resulting splittings and interactions were fit to a triplet effective spin Hamiltonian providing the zero-field splitting $D_{xy}$ for the $d_{xy}$ excited state. Both this and the ground-state $D_{x^2-y^2}$ have been related to the anisotropy in the exchange interactions between different orbital pathways determined above. These studies provide significant insight into the orbital origin of spin Hamiltonian parameters in copper dimers.

Understanding the magnetic and spectral consequences of weak interactions between metal ions has been a historical goal in physical inorganic chemistry, which has recently gained additional significance based on the presence of metal ion cluster sites in biological systems. Cluster active sites with copper, iron, and manganese, in particular, exhibit unique ground- and excited-state spectral features which appear to be associated with the interactions between metal ions.

Past research on weakly coupled transition-metal dimer systems has traditionally focused on the ground state magnetic properties.[1,2] The observed antiferromagnetic or ferromagnetic behavior is usually described by the phenomenological spin Hamiltonian[3]

$$\mathbf{H} = -2J\hat{\mathbf{S}}_1\cdot\hat{\mathbf{S}}_2 + \hat{\mathbf{S}}_1\cdot\bar{\bar{\mathbf{D}}}\cdot\hat{\mathbf{S}}_2 \quad (1)$$

where $\hat{\mathbf{S}}_1$ and $\hat{\mathbf{S}}_2$ are local spin operators on metal centers 1 and 2. $J$ is a scalar representing the isotropic exchange splitting between the total spin sublevels of the dimer ground-state manifold. The physical basis of $J$ has been interpreted in terms of superexchange interactions of the half-occupied magnetic orbitals through orbitals on the bridging ligand. Simple molecular orbital models[4,5] have been developed that allow the sign and magnitude of $J$ to be predicted by considering overlaps and energy differences of molecular orbitals. The tensor, $\mathbf{D}$, represents the zero-field splitting within a total spin substate that is due to spin dipolar and anisotropic exchange interactions[3,6] between different valence orbitals. In particular, the large zero-field splitting observed in Cu(II) dimers ($\mathbf{D} \sim 1\ cm^{-1}$) has been mostly attributed to anisotropic exchange (eq 2) involving $J_{n,x^2-y^2}$, the exchange interaction

$$D^{ex}_{x^2-y^2} = -1/16(g^{gs}_{\parallel} - 2)^2 J_{xy,x^2-y^2} + 1/4(g^{gs}_{\perp} - 2)^2 J_{xzyz,x^2-y^2} \quad (2)$$

between an electron in the $d_{x^2-y^2}$ ground state and another in a $d_n$ excited state.[1,7] However, the inability to measure the excited-state exchange interaction $J_{n,x^2-y^2}$ has prevented a critical test of this mechanism. Magneto-structural correlations[8] have been developed that explain the observed dependence of the magnitude and sign of $J$[9] and $\mathbf{D}$[10,38c] based on the geometry and type of bridging ligand. Coupled with the MO models for exchange interactions, the magneto-structural correlations provide a basis for predicting the interactions in new dimer systems. Much of the research in this area has focused on Cu(II) dimers, which have highly anisotropic half-occupied $d_{x^2-y^2}$ orbitals on each copper in the ground state. The prototype copper dimer has been the $D_{4h}$ copper acetate system pictured in Figure 1.

The excited states of binuclear metal complexes have also been recognized to exhibit effects due to dimer interactions. New absorption bands present only for pairs of interacting metal ions were observed in $PrCl_3$ and assigned as a simultaneous pair excitation (SPE) process where one photon excites f → f transitions in two metal centers through their exchange interaction.[11] Binuclear transition-metal systems such as copper[12-14] and iron-oxo[15] dimers are also known to have "dimer" bands not present in the monomer spectrum. Several possible assignments for these bands have been considered including d → d simultaneous pair excitation and low-energy charge-transfer transitions. With respect to d → d transitions, intensity enhancement of the spin-forbidden ligand

(1) Bleaney, B.; Bowers, K. D. *Proc. R. Soc. London, A* **1952**, *214*, 451-465.
(2) (a) Hatfield, W. E. In *Extended Interactions between Metal Ions in Transition Metal Complexes*; Interrante, L. V., Ed.; American Chemical Society: Washington, DC, 1974; pp 108-141. (b) Ginsberg, A. P. *Inorg. Chim. Acta Rev.* **1971**, *5*, 45-68. (c) Keijers, C. P. In *Electron Spin Resonance*; Symons, M. C. R., Ed.; (Specialist Periodical Reports), The Chemical Society, London, 1987; Vol. 10B, pp 1-38. (d) Kahn, O. In *Magneto-Structural Correlations in Exchange Coupled Systems*; Willet, R. D., Gatteschi, D., Kahn, O., Eds.; D. Reidel: Dordecht, The Netherlands, 1985; pp 37-56.
(3) (a) Moriya, T. *Phys. Rev.* **1960**, *120*, 91-98. (b) Moriya, T. In *Magnetism*; Rado, G. T., Suhl, H., Eds.; Academic Press: New York, 1963; Vol. 1, pp 85-125.
(4) Hay, P. J.; Thibeault, J. C.; Hoffmann, R. *J. Am. Chem. Soc.* **1975**, *97*, 4884-4899.
(5) (a) Kahn, O.; Briat, B. *J. Chem. Soc., Faraday Trans. 2* **1976**, *72*, 268-281; (b) *Ibid.* 1441-1446.
(6) Kanamori, J. In *Magnetism*; Rado, G. T., Suhl, H., Eds.; Academic Press: New York, 1963; Vol. 1, pp 127-203.
(7) Owen, J.; Harris, E. A. In *Electron Paramagnetic Resonance*; Geschwind, S., Ed.; Plenum: New York, 1972; pp 427-492.
(8) Willet, R. D.; Gatteschi, D.; Kahn, O., Eds. *Magneto-Structural Correlations in Exchange Coupled Systems*; D. Reidel: Dordecht, The Netherlands, 1985.
(9) (a) Hodgson, D. J. In *Magneto-Structural Correlations in Exchange Coupled Systems*; Willet, R. D., Gatteschi, D., Kahn, O., Eds.; D. Reidel: Dordecht, The Netherlands, 1985; pp 497-522. (b) Hatfield, W. E. *Ibid.* pp 555-602.
(10) (a) Bencini, A.; Gatteschi, D.; Zanchini, C.; Hasse, W. *Inorg. Chem.* **1985**, *24*, 3485-3486. (b) Bencini, A.; Gatteschi, D.; Zanchini, C. *Inorg. Chem.* **1985**, *24*, 700-703.
(11) (a) Varsanyi, F. L.; Dieke, G. H. *Phys. Rev. Lett.* **1961**, *7*, 442-443. (b) Dieke, G. H.; Dorman, E. *Ibid.* **1973**, *11*, 17-18. (c) Dexter, D. L. *Phys. Rev.* **1962**, *126*, 1962. (d) Shinagawa, K. *J. Phys. Soc. Jpn.* **1967**, *23*, 1057-1062.
(12) Hansen, A. E.; Ballhausen, C. J. *Trans. Faraday Soc.* **1965**, *61*, 631-639.
(13) Dubicki, L. *Aust. J. Chem.* **1972**, *25*, 1141-1149.
(14) Desjardins, S. R.; Wilcox, D. E.; Musselman, R. L.; Solomon, E. I. *Inorg. Chem.* **1987**, *26*, 288-300.
(15) (a) Schugar, H. J.; Rossman, G. R.; Barraclough, C. G.; Gray, H. B. *J. Am. Chem. Soc.* **1972**, *94*, 2683-2690. (b) Schugar, H. J.; Rossman, G. R.; Thibeault, J.; Gray, H. B. *Chem. Phys. Lett.* **1970**, *6*, 26.

0002-7863/89/1511-4009$01.50/0 

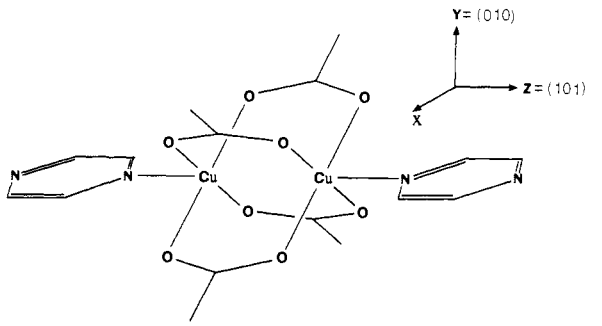


**Figure 1.** Molecular structure of copper acetate pyrazine shown with respect to the molecular axes and the crystallographic (010) and (101) directions.

field transitions of Mn(II), Cr(III), and other dimer combinations is a well-known effect of binuclear interactions.[16] Further, energy splittings of the $^2E$ excited states in Cr(III) and the $^4A,E$ excited states in Mn(II) compounds have been observed and analyzed in terms of exchange interactions.[17] The spin Hamiltonian formalism can be successfully applied to these ligand field excited-state interactions since the transitions involve only electron spin flips with no change in orbital occupation. However, the spin Hamiltonian formalism does not provide a description of the exchange interactions of excited states with different orbital electron configurations. This is the case for all excited states in Cu(II) dimers, where it will be shown that the dimer splittings of each $d_n$ excited state will depend on exchange interactions of the form $J_{n,x^2-y^2}$ and $J_{n,n}$, where n is a copper d orbital that is not $d_{x^2-y^2}$. Excited-state splittings in copper dimers, therefore, provide an opportunity to probe individual superexchange pathways between different combinations of valence orbitals.

In order to characterize the effects of binuclear interactions on excited states, we have undertaken a detailed spectroscopic study of the pyrazine salt of copper acetate. In copper acetate pyrazine, the singlet component of the ground state is 325 $cm^{-1}$ below the triplet component due to an antiferromagnetic interaction attributed to superexchange of $d_{x^2-y^2}$ electrons through the bridging acetates.[18,19] In addition, the interaction between dimers has been evaluated to be less than 0.1 $cm^{-1}$ and can therefore be neglected.[20] In the present study we have used a variety of magneto-optical techniques including linearly polarized absorption, transverse and longitudinal Zeeman, and variable-temperature magnetic circular dichroism (MCD) to observe and assign 10 individual components of the ligand field excited states and measure their energy splittings. The pyrazine salt crystallizes with molecular directions aligned along the birefringent axes, thus allowing pure molecularly polarized absorption spectra to be obtained. MCD transitions from the thermally occupied triplet component of the ground state involve $C_0$ terms and thus are inherently more intense than transitions from the singlet component of the ground state. Therefore, the variable-temperature MCD spectra complement the linearly polarized absorption spectra by providing observable triplet–triplet transitions. Copper acetate pyrazine also exhibits sharp vibronic structure on a low-energy ligand field band,[21] which we have studied in detail with transverse and longitudinal Zeeman perturbations to obtain the excited-state spin Hamiltonian parameters.

This spectral study provides important new insight into the factors contributing to excited-state splittings and allows us to probe individual exchange interactions between different valence orbitals while maintaining the same ligand environment (Figure 1). We have also experimentally evaluated the anisotropic exchange mechanism for zero-field splitting and have confirmed a singlet ligand-to-metal charge-transfer assignment of the copper acetate dimer band which is greatly lowered in energy due to large antiferromagnetic exchange interactions in specific charge-transfer excited states.

## Experimental Section

Copper acetate pyrazine crystallizes in the $C2/m$ space group[22] with two dimers per monoclinic unit cell ($a$ = 7.9156 Å, $b$ = 14.025 Å, and $c$ = 7.3022 Å; $\beta$ = 100.99°). The structure consists of linear chains of binuclear copper acetate units linked by pyrazine ligands. The crystallographic symmetry of the dimer is $C_{2h}$ with the 2-fold axis bisecting the acetate groups ($y$ in Figure 1). The molecular coordinate system is defined with $z$ along the Cu–Cu direction, $y$ along the 2-fold (010) axis, and $x$ lying in the crystallographic mirror plane and mutually perpendicular to the molecular $y$ and $z$ axes. This choice of molecular axes places the $z$ direction only 0.22° away from the (101) spindle axis of the unit cell,[23] and $x$ and $y$ bisecting the O–Cu–O angles as shown in Figure 1.

The magnetic properties of single crystals of copper acetate pyrazine have been previously reported.[22] The ground state of the dimer is antiferromagnetically coupled with $-2J$ = 325 $cm^{-1}$. EPR studies of the triplet component of the ground state give spin Hamiltonian values of $g_\parallel$ = 2.350, $g_\perp$ = 2.064, $\mathbf{D}$ = 0.329 $cm^{-1}$, and $\mathbf{E}$ = 0.0005 $cm^{-1}$. The magnetic data indicate that copper acetate pyrazine is the most nearly axial of any known copper carboxylate dimer[22] validating a $D_{4h}$ effective symmetry with the principle direction along the Cu–Cu axis.

Single crystals of copper acetate pyrazine were prepared as in ref 20. The crystals were allowed to grow for several weeks to obtain large crystals suitable for spectroscopy. Single crystals were oriented, mounted on a quartz disk, and polished to varying thicknesses generally between 10 and 100 μm along either the $\{10\bar{1}\}$ plane ($\alpha$ face) or normal to the (101) spindle axis ($\gamma$ face). The $\gamma$ face contains the $x$ and $y$ axes, while the $\alpha$ face contains the $y$ and $z$ axes. The extinction directions of these faces are symmetry restricted to lie parallel and perpendicular to the $y$ (010) axis, allowing pure molecular $x$, $y$, and $z$ polarizations to be obtained.

Linearly polarized, single-crystal absorption spectra were obtained between 5 and 300 K by using a McPherson RS-10 double-beam spectrometer with focusing optics and a Janis Super Vari-Temp helium Dewar as previously described.[24] The samples were aligned with a polarizing microscope, and polarization of the light beam to within ±1° of the extinction direction of the crystal was accomplished by using a matched pair of Glan-Taylor calcite prism polarizers. Polarized longitudinal and transverse Zeeman spectra were obtained by using the McPherson spectrometer in single-beam mode and an Oxford Instruments Spectromag 4 superconducting magnet/cryostat with filters and focusing optics between the light source and monochromator. To minimize the effect of magnetic field, the magnet was mounted midway between the light source and the side entrance slit of the monochromator with the PMT on the opposite side. The longitudinal and transverse Zeeman spectra were obtained with the magnetic field oriented parallel and perpendicular to the light path, respectively. All absorption spectra were digitized on an HP 7225B graphics plotter and digitizer. Variable-temperature magnetic circular dichroism spectra were obtained from Nujol mulls between quartz disks by using instrumentation and procedures previously described.[25] The Jasco J500-C spectropolarimeter has been interfaced with an IBM PC-XT using an IBM DACA interface board for instrument control and data acquisition. Unless otherwise stated, all MCD spectra were recorded with a 50 kG magnetic field and are presented with the zero-field spectrum subtracted.

(16) (a) McClure, D. S. *J. Chem. Phys.* **1963**, *39*, 2850–2855. (b) Lohr, L. L.; McClure, D. S. *J. Chem. Phys.* **1968**, *49*, 3516–3521. (c) Ferguson, J.; Guggenheim, H. J.; Tanabe, Y. *J. Phys. Soc. Jpn.* **1966**, *21*, 692–704. (d) Decurtins, S.; Gudel, H. U. *Inorg. Chem.* **1982**, *21*, 3598–3606, and references therein.

(17) (a) Huang, N. L. *Phys. Rev. B* **1970**, *1*, 945–949. (b) Dubicki, L. *Aust. J. Chem.* **1972**, *25*, 739–746.

(18) Goodgame, D. M. L.; Hill, N. J.; Marsham, D. F.; Scapoki, A. C.; Smart, M. L.; Troughton, P. G. H. *J. Chem. Soc., Chem. Commun.* **1969**, 629–630.

(19) (a) De Loth, P.; Cassoux, P.; Daudey, J. P.; Malrieu, J. P. *J. Am. Chem. Soc.* **1981**, *103*, 4007–4016. (b) Daudey, J. P.; De Loth, P.; Malrieu, J. P. In *Magneto-Structural Correlations in Exchange Coupled Systems*; Willet, R. D., Gatteschi, D., Kahn, O., Eds.; D. Reidel: Dordecht, The Netherlands, 1985; pp 37–56.

(20) Valentine, J. S.; Silverstein, A. J.; Soos, Z. G. *J. Am. Chem. Soc.* **1974**, *96*, 97–103.

(21) (a) McClure, D. S., private communication. (b) Wirth, D. A. Senior Thesis, Princeton, May 1976.

(22) Morosin, B.; Hughes, R. C.; Soos, Z. G. *Acta Crystallogr. B* **1975**, *31*, 762–770.

(23) Musselman, R. L.; Danielson, E. D.; Fitzsimmons, R. C.; Victor, P. L., unpublished research.

(24) Wilson, R. B.; Solomon, E. I. *Inorg. Chem.* **1978**, *17*, 1729–1736.

(25) (a) Allendorf, M. D. Ph.D. Thesis, Stanford University, 1987. (b) Spira-Solomon, D. J.; Allendorf, M. D.; Solomon, E. I. *J. Am. Chem. Soc.* **1986**, *108*, 5318–5328.

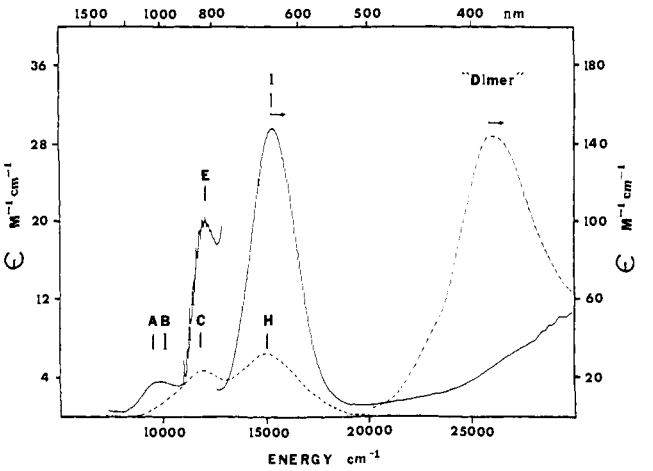


**Figure 2.** Low-temperature (5 K) molecular absorption spectra of copper acetate pyrazine polarized along the molecular $x,y$ (—), and $z$ (---) directions. The lettered positions indicate the energy of the Gaussian resolved bands. Band I and dimer intensities are defined by the right-hand scale.

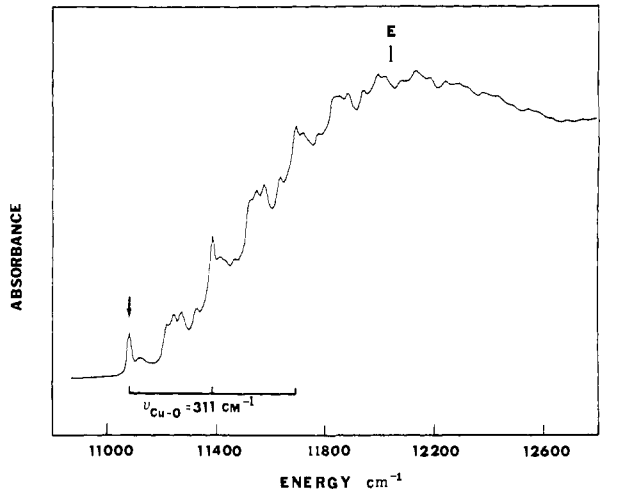


**Figure 3.** Absorption spectrum of the sharp vibronic structure on band E in the molecular $x,y$ polarization at 5 K. The progression built on the $\nu_{Cu-O}$ stretching frequency is shown with the arrow indicating the vibronic structure origin. No structure is observed in the $z$ polarization.

## Results

**Single-Crystal, Polarized Absorbance.** Linearly polarized, single-crystal absorption spectra have been taken at 5 K in the 5000–30000-cm$^{-1}$ region on the $\alpha$ and $\gamma$ faces giving spectra polarized along the molecular $x$, $y$, and $z$ axes. The $x$ and $y$ polarizations on the $\gamma$ face and the $y$ polarization on the $\alpha$ face are equivalent, confirming the axial symmetry of the complex. The $x,y$ polarization has been fit with three Gaussian bands at 10000, 12050, and 15475 cm$^{-1}$ designated A, E, and I in Figure 2. Band I at 15475 cm$^{-1}$ is the most intense ($\epsilon \simeq 150$ M$^{-1}$ cm$^{-1}$) and dominates the spectrum. The lower energy band E is much weaker ($\epsilon \simeq 20$ M$^{-1}$ cm$^{-1}$) and exhibits a series of very sharp (fwhm $\simeq 6$ cm$^{-1}$) vibronic progressions starting from an origin at 11096 cm$^{-1}$. Figure 3 gives an expanded view of the vibronic structure on band E. The most prominent progression is built upon the totally symmetric copper–oxygen breathing mode ($\nu_{Cu-O} \simeq 311$ cm$^{-1}$).[26] Other progressions appear to consist of low-frequency vibrations plus one or more quanta of $\nu_{Cu-O}$. Band A at 10000 cm$^{-1}$ in Figure 2 is weaker ($\epsilon \simeq 4$ cm$^{-1}$), broad, and featureless. No other bands are seen to lower energy in either polarization. As the temperature is increased, band I broadens and shifts to lower energy obscuring bands A and E.

(26) Mathey, Y.; Greig, D. R.; Shriver, D. F. *Inorg. Chem.* **1982**, *21*, 3409–3413.

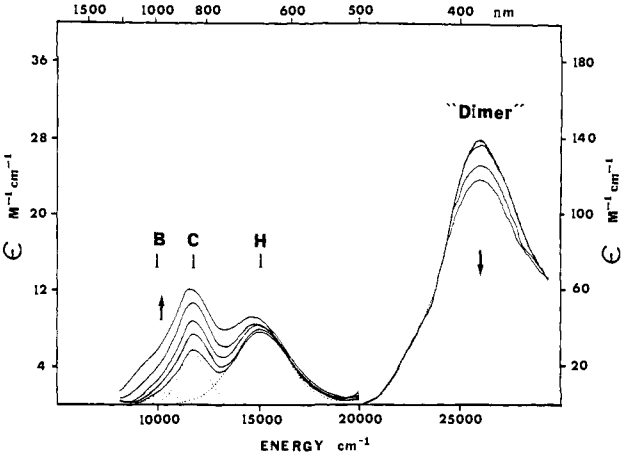


**Figure 4.** Temperature dependence of the molecular $z$ polarized absorption spectrum (—) with the Gaussian resolved bands (···) of the lowest temperature spectrum. The arrows indicate the change in intensity with increasing temperature ($T$ = 5, 50, 77, 125, 175 K). The dimer intensity is defined by the right-hand scale.

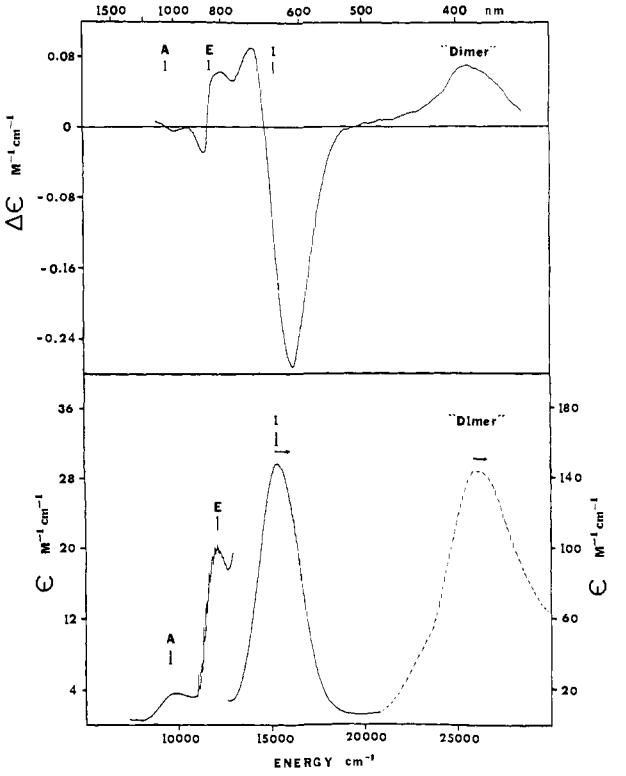


**Figure 5.** (Top) Low-temperature (5 K) MCD spectrum of a Nujol mull of copper acetate pyrazine at 50 kG with the zero-field spectrum subtracted. (Bottom) Low-temperature (5 K) molecular $x,y$ polarized (—) absorption spectrum from 500 to 1200 nm. The $z$ polarized (---) dimer band spectrum is indicated in the 500–300-nm region.

The $z$ polarized spectrum in Figure 2 is dominated by an intense band ($\epsilon \simeq 145$ M$^{-1}$ cm$^{-1}$) at 26000 cm$^{-1}$. This band is indicative of copper dimers and is denoted as the "dimer" band. As shown in Figure 4, the intensity of the strictly $z$ polarized band increases as the temperature decreases, with no significant shift in energy. The rest of the $z$ polarized spectrum has been fit with three weak bands at 10500, 11900, and 15050 cm$^{-1}$ designated B, C, and H as shown in Figure 2. The intensity of bands B and C in Figure 4 increases with increasing temperature, while band H at higher energy remains essentially constant with temperature.

**Magnetic Circular Dichroism.** The 5 K MCD spectrum of copper acetate pyrazine in a Nujol mull shows four major features in the region from 10000 to 30000 cm$^{-1}$ which is correlated with the absorption spectrum as shown in Figure 5. At highest energy there is a broad positive band that corresponds to the $z$ polarized

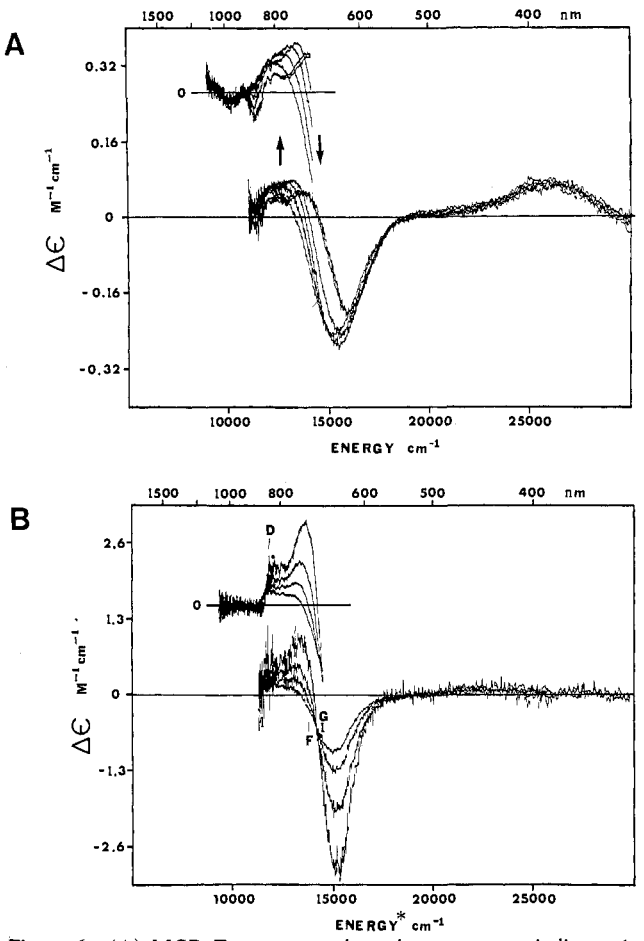


**Figure 6.** (A) MCD Temperature dependence: arrows indicate the change in MCD intensity with increasing temperature ($T$ = 5, 75, 150, 250, 300 K). Inset: low-energy data taken with the S1 PMT. (B) Temperature dependence of MCD intensity originating from the $^3A_{1u}$ ground state. The population weighted 5 K spectrum was subtracted from the higher temperature spectra in A and multiplied by $e^{+2J/kT}$ to renormalize to 100% triplet population. *The energy scale has been corrected by adding 325 cm$^{-1}$ to reference all energies to the singlet ground state.

dimer band at 26 000 cm$^{-1}$. To lower energy three skewed derivative shaped features correlate with the three $x,y$ polarized absorption bands (A, E, I). Each of the skewed derivatives is the composition of a symmetric derivative shaped $A_1$ term and a Gaussian shaped $B_0$ term. Bands A and I have negative $A_1$ and $B_0$ terms, whereas band C has a positive $A_1$ and $B_0$ term, where the sign of the $A_1$ term is given by the sign of its component to highest energy.[27]

As the temperature is increased the MCD spectrum gains positive intensity around 13 000 cm$^{-1}$ and negative intensity at 14 500 cm$^{-1}$ (Figure 6A). This temperature dependence is attributed to population of the ground-state triplet at 325 cm$^{-1}$. By subtracting the population weighted 5 K singlet ground-state spectrum and renormalizing for 100% triplet population (by multiplying by $e^{+2J/kT}$), the MCD spectrum due to the pure triplet component of the ground state can be obtained and is shown in Figure 6B for several temperatures. The wavelength scale of Figure 6B has been shifted by +325 cm$^{-1}$ to reference all high-temperature MCD triplet transition energies to transition energies from the singlet component of the ground state obtained from absorbance and low-temperature MCD. The temperature dependence of the triplet ground-state spectrum (Figure 6B) can be fit with three bands. The main portion of the spectrum is composed of two oppositely signed $C_0$ terms (bands F and G

(27) (a) Pheipho, S. B.; Schatz, P. N. *Group Theory in Spectroscopy*; Wiley: New York, 1983. (b) Stephens, P. J. *Adv. Chem. Phys.* **1976**, *35*, 197–264.

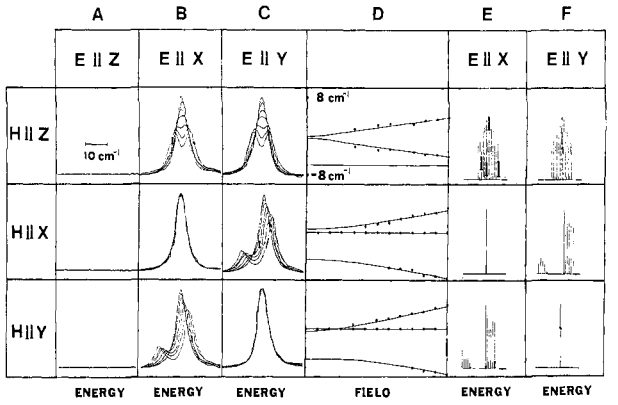


**Figure 7.** Zeeman effect on the vibronic origin indicated by the arrow in Figure 3 with light polarized along the molecular $z$ (column A), $x$ (column B), and $y$ (column C) directions and magnetic field varied from 0 to 60 kG. Column D: Magnetic field dependence of Gaussian resolved bands (●) with best fit to the triplet spin Hamiltonian (—), eq 13. Columns E and F: Field dependent intensity of triplet spin components polarized along the $x$ and $y$ molecular directions calculated from the best fit triplet spin Hamiltonian parameters. Intensities with $\mathbf{H}\|z$ have been weighted to account for overlap of levels with finite band width.

centered at 14 275 and 14 975 cm$^{-1}$) overlapping to form a "pseudo" $A_1$ term. A negative $B_0$ term drops the isosbestic point below zero. The third band (D) is a weak positive $C_0$ term at 11 950 cm$^{-1}$. No further bands are observed to lower energy in the MCD spectrum. It is important to note that the high-temperature MCD spectrum exhibits no band in the dimer region of the spectrum.

**Zeeman Spectra of the Structured Origin.** Figure 3 shows an expanded view of the vibronic structure on band C. Transverse and longitudinal Zeeman spectra of the vibronic structured origin (indicated by the arrow in Figure 3) were obtained on both faces with the magnetic field along the $x$, $y$, and $z$ molecular axes. In the transverse Zeeman experiment with the magnetic field along the $x$ or $y$ directions and the light polarized with $\vec{E}$ along the magnetic field, no field dependence was seen (Figure 7, B middle, C bottom). When the light was polarized perpendicular to the field, the single-origin peak split asymmetrically into two bands with unequal intensity (Figure 7, B bottom, C middle). With the magnetic field along the $z$ molecular direction and the light polarized perpendicular to $z$, the origin split symmetrically into two peaks with equal intensity (Figure 7, B and C top). Since the band is $x,y$ polarized, no feature is observed with the light polarized along $z$ (Figure 7A). The energy splittings of the band are plotted as a function of magnetic field strength in the Figure 7D.

## Analysis

**Dimer States: Wave Functions and Energies.** Weakly coupled transition-metal dimer systems can be treated by the coupled chromophore model of Ballhausen and Hansen.[12] The dimer wave functions are composed of linear combinations of Slater determinants formed from one-electron spin–orbitals localized one each $C_{4v}$ monomeric fragment. Table IA lists the wave functions of the ground state and those corresponding to single-site excitations.[28] Each ligand field excited state of the monomer generates a singlet and triplet state in the dimer. The three spin components of the ground-state triplet (denoted by a superscript +, −, or 0) are given explicitly in Table IA, while for brevity only the $m_s$ = +1 component is given for each single-site triplet excitation. The wave function denoted by $\psi_1$ corresponds to a $b_1 \rightarrow a_1$ excitation on the copper 1 monomer, while $\psi_2$ corresponds to this excitation on copper 2. Symmetric and antisymmetric combinations of the singlets and triplets that have the complete $D_{4h}$ symmetry of the

(28) The orbitals are designated by their transformations in $C_{4v}$, the superscripts refer to the Cu fragment (1 or 2) on which the oribtal is localized, and the subscripts a and b refer to the $xz$, and $yz$ orbital components of the doubly degenerate e states. The notation of the determinants is simplified by using the hole notation, where a bar over an orbital denotes a $\beta$ spin hole and the absence of a bar denotes an $\alpha$ spin hole.

**Table I.**[a] Coupled Chromophore Wave Functions of Ligand Field States

(A) Ground-State Components

| | | |
|---|---|---|
| $x^2-y^2$ | $^1\psi_0 = 1/\sqrt{2}\{\|b_1^1\bar{b}_1^2\| - \|\bar{b}_1^1 b_1^2\|\}$ | |
| | $^3\psi_0^+ = \|b_1^1 b_1^2\|$ | |
| | $^3\psi_0^0 = 1/\sqrt{2}\{\|b_1^1\bar{b}_1^2\| + \|\bar{b}_1^1 b_1^2\|\}$ | |
| | $^3\psi_0^- = \|\bar{b}_1^1\bar{b}_1^2\|$ | |
| | Single-Site Excitations | |
| $z^2$ | $^1\psi_1 = 1/\sqrt{2}\{\|a_1^1\bar{b}_1^2\| - \|\bar{a}_1^1 b_1^2\|\}$ | |
| | $^3\psi_1 = \|a_1^1 b_1^2\|$ | |
| | $^1\psi_2 = 1/\sqrt{2}\{\|b_1^1\bar{a}_1^2\| - \|\bar{b}_1^1 a_1^2\|\}$ | |
| | $^3\psi_2 = \|b_1^1 a_1^2\|$ | |
| $xy$ | $^1\psi_3 = 1/\sqrt{2}\{\|b_2^1\bar{b}_1^2\| - \|\bar{b}_2^1 b_1^2\|\}$ | |
| | $^3\psi_3 = \|b_2^1 b_1^2\|$ | |
| | $^1\psi_4 = 1/\sqrt{2}\{\|b_1^1\bar{b}_2^2\| - \|\bar{b}_1^1 b_2^2\|\}$ | |
| | $^3\psi_4 = \|b_1^1 b_2^2\|$ | |
| $xz,yz$ | $^1\psi_5 = 1/\sqrt{2}\{\|e_a^1\bar{b}_1^2\| - \|\bar{e}_a^1 b_1^2\|\}$ | |
| | $^3\psi_5 = \|e_a^1 b_1^2\|$ | |
| | $^1\psi_6 = 1/\sqrt{2}\{\|e_b^1\bar{b}_1^2\| - \|\bar{e}_b^1 b_1^2\|\}$ | |
| | $^3\psi_6 = \|e_b^1 b_1^2\|$ | |
| | $^1\psi_7 = 1/\sqrt{2}\{\|b_1^1\bar{e}_a^2\| - \|\bar{b}_1^1 e_a^2\|\}$ | |
| | $^3\psi_7 = \|b_1^1 e_a^2\|$ | |
| | $^1\psi_8 = 1/\sqrt{2}\{\|b_1^1\bar{e}_b^2\| - \|\bar{b}_1^1 e_b^2\|\}$ | |
| | $^3\psi_8 = \|b_1^1 e_b^2\|$ | |

(B) Dimer Ground State: $D_{4h}$

| | | |
|---|---|---|
| $x^2-y^2$ | $^1\Phi_0 = {}^1\psi_0$ | $^1A_{1g}$ |
| | $^3\Phi_0^+ = {}^3\psi_0^+$ | $^3A_{2u}$ |
| | $^3\Phi_0^0 = {}^3\psi_0^0$ | $^3A_{2u}$ |
| | $^3\Phi_0^- = {}^3\psi_0^-$ | $^3A_{2u}$ |
| | Dimer Excited States: $D_{4h}$ | |
| $z^2$ | $^1\Phi_1 = 1/\sqrt{2}\{^1\psi_1 + {}^1\psi_2\}$ | $^1B_{1g}$ |
| | $^1\Phi_2 = 1/\sqrt{2}\{^1\psi_1 - {}^1\psi_2\}$ | $^1B_{2u}$ |
| | $^3\Phi_1 = 1/\sqrt{2}\{^3\psi_1 + {}^3\psi_2\}$ | $^3B_{2u}$ |
| | $^3\Phi_2 = 1/\sqrt{2}\{^3\psi_1 - {}^3\psi_2\}$ | $^3B_{1g}$ |
| $xy$ | $^1\Phi_3 = 1/\sqrt{2}\{^1\psi_3 + {}^1\psi_4\}$ | $^1A_{2g}$ |
| | $^1\Phi_4 = 1/\sqrt{2}\{^1\psi_3 - {}^1\psi_4\}$ | $^1A_{1u}$ |
| | $^3\Phi_3 = 1/\sqrt{2}\{^3\psi_3 + {}^3\psi_4\}$ | $^3A_{1u}$ |
| | $^3\Phi_4 = 1/\sqrt{2}\{^3\psi_3 - {}^3\psi_4\}$ | $^3A_{2g}$ |
| $xz,yz$ | $^1\Phi_5 = 1/\sqrt{2}\{^1\psi_5 + {}^1\psi_7\}$ | $^1E_g(xz)$ |
| | $^1\Phi_6 = 1/\sqrt{2}\{^1\psi_6 + {}^1\psi_8\}$ | $^1E_g(yz)$ |
| | $^1\Phi_7 = 1/\sqrt{2}\{^1\psi_5 - {}^1\psi_7\}$ | $^1E_u(xz)$ |
| | $^1\Phi_8 = 1/\sqrt{2}\{^1\psi_6 - {}^1\psi_8\}$ | $^1E_u(yz)$ |
| | $^3\Phi_5 = 1/\sqrt{2}\{^3\psi_5 + {}^3\psi_7\}$ | $^3E_u(xz)$ |
| | $^3\Phi_6 = 1/\sqrt{2}\{^3\psi_6 + {}^3\psi_8\}$ | $^3E_u(yz)$ |
| | $^3\Phi_7 = 1/\sqrt{2}\{^3\psi_5 - {}^3\psi_7\}$ | $^3E_g(xz)$ |
| | $^3\Phi_8 = 1/\sqrt{2}\{^3\psi_6 - {}^3\psi_8\}$ | $^3E_g(yz)$ |

(C) Orbitally Degenerate Spin–Orbit Dimer States: $D_{4h}'$

| | | |
|---|---|---|
| $^1E_g$ | $^1\Psi_5 = {}^1\Phi_5$ | $\Gamma_5^+$ |
| | $^1\Psi_6 = {}^1\Phi_6$ | $\Gamma_5^+$ |
| $^1E_u$ | $^1\Psi_7 = {}^1\Phi_7$ | $\Gamma_5^-$ |
| | $^1\Psi_8 = {}^1\Phi_8$ | $\Gamma_5^-$ |
| $^3E_u$ | $^3\Psi_5 = 1/2\{^3\Phi_5^+ - {}^3\Phi_5^- + i^3\Phi_6^+ + i^3\Phi_6^-\}$ | $\Gamma_1^-$ |
| | $^3\Psi_6 = 1/2\{^3\Phi_5^+ + {}^3\Phi_5^- + i^3\Phi_6^+ - i^3\Phi_6^-\}$ | $\Gamma_2^-$ |
| | $^3\Psi_7 = {}^3\Phi_5^0$ | $\Gamma_5^-$ |
| | $^3\Psi_8 = {}^3\Phi_6^0$ | $\Gamma_5^-$ |
| | $^3\Psi_9 = 1/2\{^3\Phi_5^+ - {}^3\Phi_5^- - i^3\Phi_6^+ - i^3\Phi_6^-\}$ | $\Gamma_3^-$ |
| | $^3\Psi_{10} = 1/2\{^3\Phi_5^+ + {}^3\Phi_5^- - i^3\Phi_6^+ + i^3\Phi_6^-\}$ | $\Gamma_4^-$ |
| $^3E_g$ | $^3\Psi_{11} = 1/2\{^3\Phi_7^+ + {}^3\Phi_7^- + i^3\Phi_8^+ - i^3\Phi_8^-\}$ | $\Gamma_1^+$ |
| | $^3\Psi_{12} = 1/2\{^3\Phi_7^+ - {}^3\Phi_7^- + i^3\Phi_8^+ + i^3\Phi_8^-\}$ | $\Gamma_2^+$ |
| | $^3\Psi_{13} = {}^3\Phi_7^0$ | $\Gamma_5^+$ |
| | $^3\Psi_{14} = {}^3\Phi_8^0$ | $\Gamma_5^+$ |
| | $^3\Psi_{15} = 1/2\{^3\Phi_7^+ + {}^3\Phi_7^- - i^3\Phi_8^+ + i^3\Phi_8^-\}$ | $\Gamma_3^+$ |
| | $^3\Psi_{16} = 1/2\{^3\Phi_7^+ - {}^3\Phi_7^- - i^3\Phi_8^+ - i^3\Phi_8^-\}$ | $\Gamma_4^+$ |

(D) Orbitally Degenerate Zeeman Dimer States: $C_{4h}'$

| | | |
|---|---|---|
| $^1E_g$ | $^1\theta_5 = 1/\sqrt{2}\{^1\Phi_5 + i^1\Phi_6\}$ | $\Gamma_4^+$ |
| | $^1\theta_6 = 1/\sqrt{2}\{^1\Phi_5 - i^1\Phi_6\}$ | $\Gamma_3^+$ |
| $^1E_u$ | $^1\theta_7 = 1/\sqrt{2}\{^1\Phi_7 + i^1\Phi_8\}$ | $\Gamma_4^-$ |
| | $^1\theta_8 = 1/\sqrt{2}\{^1\Phi_7 - i^1\Phi_8\}$ | $\Gamma_3^-$ |
| $^3E_u$ | $^3\theta_5 = 1/\sqrt{2}\{^3\Phi_5^+ + i^3\Phi_6^+\}$ | $\Gamma_1^-$ |
| | $^3\theta_6 = 1/\sqrt{2}\{^3\Phi_5^- - i^3\Phi_6^-\}$ | $\Gamma_1^-$ |
| | $^3\theta_7 = 1/\sqrt{2}\{^3\Phi_5^0 + i^3\Phi_6^0\}$ | $\Gamma_4^-$ |
| | $^3\theta_8 = 1/\sqrt{2}\{^3\Phi_5^0 - i^3\Phi_6^0\}$ | $\Gamma_3^-$ |
| | $^3\theta_9 = 1/\sqrt{2}\{^3\Phi_5^+ - i^3\Phi_6^+\}$ | $\Gamma_2^-$ |
| | $^3\theta_{10} = 1/\sqrt{2}\{^3\Phi_5^- + i^3\Phi_6^-\}$ | $\Gamma_2^-$ |
| $^3E_g$ | $^3\theta_{11} = 1/\sqrt{2}\{^3\Phi_7^+ + i^3\Phi_8^+\}$ | $\Gamma_1^+$ |
| | $^3\theta_{12} = 1/\sqrt{2}\{^3\Phi_7^- - i^3\Phi_8^-\}$ | $\Gamma_1^+$ |
| | $^3\theta_{13} = 1/\sqrt{2}\{^3\Phi_7^0 + i^3\Phi_8^0\}$ | $\Gamma_4^+$ |
| | $^3\theta_{14} = 1/\sqrt{2}\{^3\Phi_7^0 - i^3\Phi_8^0\}$ | $\Gamma_3^+$ |
| | $^3\theta_{15} = 1/\sqrt{2}\{^3\Phi_7^+ - i^3\Phi_8^+\}$ | $\Gamma_2^+$ |
| | $^3\theta_{16} = 1/\sqrt{2}\{^3\Phi_7^- + i^3\Phi_8^-\}$ | $\Gamma_2^+$ |

[a] For all nondegenerate states $\Phi_i = \Psi_i = \theta_i$.

dimer will generate a total of four dimer excited states for each monomer excited state. These wave functions are listed in Table IB. For example, the monomer $d_{z^2}$ excited state generates four dimer states which transform as $^1B_{1g}$, $^1B_{2u}$, $^3B_{1g}$, and $^3B_{2u}$ in $D_{4h}$ dimer symmetry. The splittings of each single ion d–d state into dimer states is given in column B of Figure 8; the magnitude of the energy splittings between the states will be discussed in the resonance splitting section (vide infra).

The $^3E_g$ and $^3E_u$ states both have in-state orbital angular momentum in $D_{4h}$ and thus will further split into three double-degenerate states due to spin–orbit coupling. The spin–orbit Hamiltonian for the dimer is a sum of single-center, one-electron operators and is given by

$$\mathbf{H}_{s.o.} = \sum_i \sum_j \xi_j \hat{l}_{ij} \cdot \hat{s}_{ij} \qquad (3)$$

where $i$ and $j$ sum over the electron and copper coordinates. In the limit of neglect of overlap (no contribution of center 2 from an operator located on center 1), evaluation of the spin–orbit Hamiltonian (eq 3) over all of the dimer-state wave functions given in Table I, parts B and C, gives the spin–orbit matrix elements included in the Supplementary Material in Tables S1 and S2. Linear combinations of the $^3E_g$ and $^3E_u$ states that diagonalize the spin–orbit Hamiltonian in the $D_{4h}'$ double group are listed in Table IC. The energy splittings of the $^3E_g$ and $^3E_u$ spin–orbit components and the transformation properties of all the dimer states in $D_{4h}'$ symmetry are summarized in column C of Figure 8.

In order to determine the MCD selection rules, the effect of a magnetic field on the dimer states must be evaluated. The MCD selection rules require a transition to be polarized in two directions mutually perpendicular to the magnetic field (vide infra). Therefore, in first order the $z$ polarized transitions will not contribute to the MCD, and the $x,y$ polarized transitions will only contribute when the magnetic field is along the molecular $z$ axis. An external magnetic field along $z$ will lower the effective symmetry of the dimer to $C_{4h}'$. All of the orbitally nondegenerate dimer states in Table IB are diagonal in the magnetic field and will split based on $m_s$ component. However, the orbital degenerate states have angular momentum and will be mixed by the field. Linear combinations of the orbitally degenerate dimer states that diagonalize the Zeeman Hamiltonian are given in Table ID. The Zeeman Hamiltonian is given by

$$\mathbf{H}_{zee} = \sum_{ij} (\hat{l}_{ij} + 2\hat{s}_{ij}) \qquad (4)$$

where $i$ and $j$ sum over the electron and copper coordinates. Operating the Zeeman Hamiltonian on the nondegenerate dimer states in Table IB and the degenerate dimer states in Table ID gives the energy corrections that are listed in column D of Figure 8 along with their transformation properties in $C_{4h}'$ symmetry. Orbitally nondegenerate triplet states split symmetrically in a magnetic field with the $m_s = +1$ component always to higher energy. For states with orbital angular momentum, the splitting is derived from a combination of the angular and spin momentum, as seen for the $^3E_u$ and $^3E_g$ states in column D of Figure 8.

**Selection Rules.** A summary of all groups theoretically allowed, linearly polarized transitions, and their selection rules is given in Table II, columns 4–6. The $x$ and $y$ electric dipole operators transform together as $e_u$ in $D_{4h}$ symmetry, while the $z$ operator transforms as $a_{2u}$. In low-temperature absorption spectroscopy the only spin allowed, electric dipole allowed transition originating from the $^1A_{1g}$ component of the ground state is the $x,y$ polarized $^1A_{1g} \rightarrow {}^1E_u$, which corresponds (Table I) to an antisymmetric

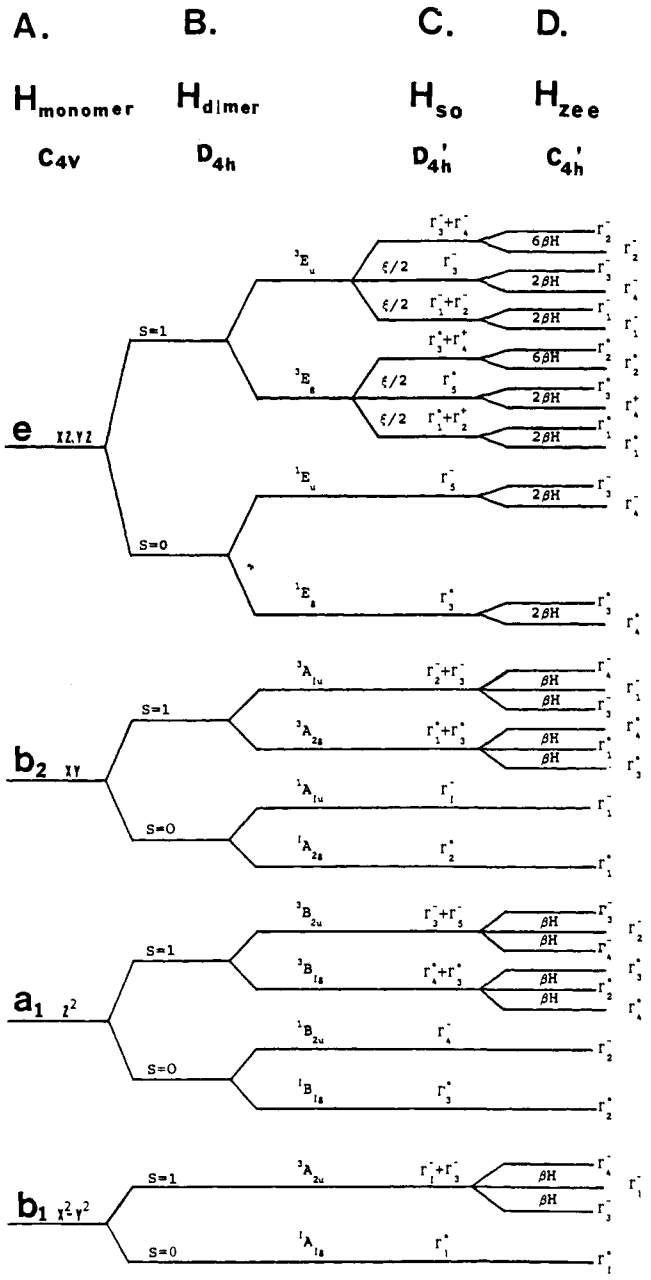


Figure 8. Energy level diagram for copper acetate. Column A: Splitting of copper d orbitals in the effective $C_{4v}$ symmetry of the monomer. Column B: Dimer states in $D_{4h}$ symmetry. Column C: Effect of spin–orbit coupling in $D_{4h}'$ symmetry. Column D: Effect of an axial magnetic field in $C_{4h}'$ symmetry.

combination of excitations of one electron from the $d_{xz,yz}$ orbital of a cupric ion into the $d_{x^2-y^2}$ orbital (see column 4 in Table II).

Other states can gain intensity by spin–orbit coupling to the $^1E_u$ excited state or to an allowed charge-transfer excited state. Since $^1E_u$ transforms as $\Gamma_5^-$ in the $D_{4h}'$ double group, components of the $^3B_{2u}$, $^3A_{1u}$, and $^3E_u$ excited states that also transform as $\Gamma_5^-$ are group theoretically allowed to gain $x,y$ polarized absorption intensity. Likewise, the $^3A_{1u}(\Gamma_2^-)$ and $^3E_u(\Gamma_2^-)$ excited states are allowed to gain $z$ polarized absorption intensity by mixing with charge-transfer transitions that transform as $\Gamma_2^-$. The selection rules of all transitions made allowed by spin–orbit coupling are given in the fifth column of Table II.

Another mechanism for states to gain absorption intensity is through vibronic coupling. Vibronic coupling allows excited states to mix with other electric dipole allowed states through an additional spin-independent term in the Hamiltonian that couples the electron and nuclear motions. The orbitally forbidden singlet excited states that are vibronically allowed in $x,y$ and $z$ polarizations are listed in column 6 of Table II along with the allowing vibrational normal mode. Note that all singlet states become allowed except the $^1A_{1u}$ in $z$ polarization.

In low-temperature MCD spectroscopy, transitions originating from the $^1A_{1g}$ component of the ground state will contribute temperature-independent $A_1$ and $B_0$ terms. The $B_0$ terms originate from field-induced mixing summed over all excited states and will not be evaluated. The $A_1$ terms arise from transitions from a nondegenerate ground state to orbitally degenerate excited states. Equation 5

$$\bar{A}_1 = \frac{-i}{3\beta|A|}\sum_{\alpha\alpha'\lambda\lambda'}(\langle J\lambda|\mu|J\lambda'\rangle\delta_{\alpha\alpha'} - \langle A\alpha|\mu|A\alpha'\rangle\delta_{\gamma\gamma'})\cdot \langle A\alpha'|\mathbf{m}|J\lambda\rangle\times\langle J\lambda|\mathbf{m}|A\alpha\rangle \quad (5)$$

expresses the orientationally averaged intensity[27] of the $A_1$ term as a sum of Zeeman and electric dipole matrix elements, where $A\alpha$ and $J\lambda$ represent components of the ground and excited states, $\mu$ is the magnetic dipole operator, $\mathbf{m}$ is the electric dipole operator, and $|A|$ is the degeneracy of the ground state. As can be seen from eq 5, only transitions that have two electric dipole allowed polarizations perpendicular to the magnetic field will contribute to the MCD spectrum. Therefore, only the $x,y$ polarized transitions will contribute to the intensity of the $A_1$ term, and eq 5 can be simplified[27] to give

$$A_1 = \frac{1}{|A|}\sum_{\alpha\lambda}(\langle J\lambda|\mathbf{L}_z + 2\mathbf{S}_z|J\lambda\rangle - \langle A\alpha|\mathbf{L}_z + 2\mathbf{S}_z|A\alpha\rangle)\times (|\langle J\lambda|\mathbf{m}_{+1}|A\alpha\rangle|^2 - |\langle J\lambda|\mathbf{m}_{-1}|A\alpha\rangle|^2) \quad (6)$$

where $\mathbf{m}_{-1}$ and $\mathbf{m}_{+1}$ represent the left and right circularly polarized electric dipole operators, respectively. The sign of the $A_1$ term can be determined by evaluating which of the $\mathbf{m}_{+1}$ and $\mathbf{m}_{-1}$ matrix elements in eq 6 will be nonzero.

At low temperatures, the MCD transitions of interest are from the $^1A_{1g}(\Gamma_1^+)$ ground state to higher excited states. In the presence of an axial magnetic field the effective symmetry is lowered to $C_{4h}'$, with the left and right circularly polarized electric dipole operators transforming as $\Gamma_4^-$ and $\Gamma_3^-$, respectively. The $C_{4h}'$ double group contains complex irreducible representations, necessitating the use of the complex conjugate of the excited-state irreducible representation when evaluating for group theoretically allowed transitions. Therefore, transitions from the $^1A_{1g}(\Gamma_1^+)$ to $\Gamma_4^-$ excited states will be left circularly polarized and transitions to $\Gamma_3^-$ excited states will be right circularly polarized. Inspection of column D in Figure 8 indicates the $^1E_u$ excited state to have a right circularly polarized transition to higher energy and a left circularly polarized transition to lower energy, resulting in a negative $A_1$ term, as listed in the seventh column of Table II. The spin components of the $^3A_{1u}$ and $^3B_{2u}$ states will spin–orbit couple to orbital components of the $x,y$ polarized $^1E_u$. The energy splittings and transformation properties in column D of Figure 8 indicate excited-state Zeeman splittings which lead to positive and negative $A_1$ terms for the $^3A_{1u}$ and $^3B_{2u}$ excited states, respectively. These spin–orbit allowed low-temperature MCD transitions are listed in column 8 of Table II.

At higher temperatures, MCD transitions will originate from the thermally populated $^3A_{2u}$ component of the ground state producing temperature-dependent $C_0$ terms, due to unequal populations within the Zeeman split triplet spin states. Again, the orientationally averaged equation can be simplified due to the $D_{4h}$ symmetry at zero field and with first-order spin–orbit coupling gives[27]

$$C_0 = \frac{-1}{|A|}\sum_{\alpha\lambda}\langle A\alpha|\mathbf{L}_z + 2\mathbf{S}_z|A\alpha\rangle\times(|\langle J\lambda|\mathbf{m}_{+1}|A\alpha\rangle|^2 - |\langle J\lambda|\mathbf{m}_{-1}|A\alpha\rangle|^2) \quad (7)$$

The only electric dipole transition allowed from the thermally populated $^3A_{2u}$ is to the $^3E_g$ state which is $x,y$ polarized and spin–orbit split into the doubly degenerate $^3\Psi_{11,12}(\Gamma_1^+,\Gamma_2^+)$, $^3\Psi_{13,14}(\Gamma_5^+)$, and $^3\Psi_{15,16}(\Gamma_3^+,\Gamma_4^+)$ states in $D_{4h}'$ symmetry. When an axial magnetic field is applied, these spin–orbit components

Table II. Predicted Excited-State Properties and Intensity Mechanisms

| | dimer states | | low-temp abs | | | low-temp MCD | | high-temp MCD | |
|---|---|---|---|---|---|---|---|---|---|
| | $D_{4h}$ | $D_{4h}'$ | E dip. | s.o. | vib | E dip. | s.o. | E dip. | s.o. |
| ground states | | | | | | | | | |
| $x^2 - y^2$ | $^1A_{1g}$ | $\Gamma_1^+$ | | | | | | | |
| | $^3A_{2u}$ | $\Gamma_1^- \Gamma_5^-$ | | | | | | | |
| excited states | | | | | | | | | |
| $z^2$ | $^3B_{2u}$ | $\Gamma_3^- \Gamma_5^-$ | | $X,Y$ | | | $-A_1$ | | |
| | $^3B_{1g}$ | $\Gamma_4^+ \Gamma_5^+$ | | | | | | | $-C_0$ |
| | $^1B_{2u}$ | $\Gamma_4^-$ | | | $X,Y(e_g)$ $Z(b_{1g})$ | | | | |
| | $^1B_{1g}$ | $\Gamma_3^+$ | | | $X,Y(e_u)$ $Z(b_{2u})$ | | | | $-C_0$ |
| $xy$ | $^3A_{1u}$ | $\Gamma_2^- \Gamma_5^-$ | | $X,Y,Z$ | | | $+A_1$ | | |
| | $^3A_{2g}$ | $\Gamma_1^+ \Gamma_5^+$ | | | | | | | $+C_0$ |
| | $^1A_{1u}$ | $\Gamma_1^-$ | | | $X,Y(e_g)$ | | | | |
| | $^1A_{2g}$ | $\Gamma_2^+$ | | | $X,Y(e_u)$ $Z(a_{2u})$ | | | | $+C_0$ |
| $xz,yz$ | $^3E_g$ | $\Gamma_1^+ \Gamma_2^+$ $\Gamma_5^+$ | | | | | | $+C_0$ | |
| | | $\Gamma_3^+ \Gamma_4^+$ | | | | | | $-C_0$ | |
| | $^3E_u$ | $\Gamma_1^- \Gamma_2^-$ | | $Z$ | | | | | |
| | | $\Gamma_5^-$ | | $X,Y$ | | | | | |
| | | $\Gamma_3^- \Gamma_4^-$ | | | | | | | |
| | $^1E_g$ | $\Gamma_5^+$ | | | $X,Y(a_{1u},a_{2u},b_{1u},b_{2u})$ $Z(e_u)$ | | | | |
| | $^1E_u$ | $\Gamma_5^-$ | $X,Y$ | | $Z(e_g)$ | $-A_1$ | | | |

split into pairs transforming as $^3\theta_{11,12}(\Gamma_1^+)$, $^3\theta_{13,14}(\Gamma_3^+,\Gamma_4^+)$, and $^3\theta_{15,16}(\Gamma_2^+)$ in $C_{4h}'$ symmetry. Inspection of column D in Figure 8 and Table ID predicts that the $m_s = -1$ component of the $^3A_{2u}(\Gamma_3^-)$ ground state will have transitions to the spin allowed $\Gamma_1^+$ and $\Gamma_2^+$ excited states being left ($\mathbf{m}_{-1} \sim \Gamma_4^-$) and right ($\mathbf{m}_{+1} \sim \Gamma_3^-$) circularly polarized, respectively. The $m_s = +1$ ground-state component will have oppositely polarized transitions, but they will be less intense due to the smaller thermal population of the higher energy $m_s = +1$ state. Since the $m_s = 0$ spin component of the $^3A_{2u}$ ground state has a zero Zeeman energy term in eq 7, transitions from the $m_s = 0$ spin state to the $^3\theta_{13,14}(\Gamma_3^+,\Gamma_4^+)$ excited state will not contribute $C_0$ term intensity to the MCD spectrum. Hence, transitions from the $^3A_{2u}$ to $^3\theta_{11,12}(\Gamma_1^+)$ and $^3\theta_{15,16}(\Gamma_2^+)$ are both allowed in $x,y$ polarization providing positive and negative $C_0$ terms, respectively, as listed in Table II, column 9. These electric dipole allowed transitions should dominate the MCD spectrum as the triplet state becomes populated at higher temperatures. Four other states can become MCD allowed through out of state spin–orbit coupling with this transition. Both $^1A_{2g}$ and $^3A_{2g}$ can couple with the $^3E_g(^3\Psi_{11,12})$ to gain positive $C_0$ term intensity, while $^1B_{1g}$ and $^3B_{1g}$ can couple to $^3E_g(^3\Psi_{15,16})$ to gain negative $C_0$ term intensity. The spin–orbit matrix elements for the $^1A_{2g}$ and $^3A_{2g}$ excited states are equal, as are those for the $^1B_{1g}$ and $^3B_{1g}$ excited states (see Supplementary Material, Table S1). Therefore, the singlet and triplet of each of these excited states are predicted to have the same intensity.

Table II summarizes the polarizations and temperature dependence for all of the group theoretically allowed absorption and MCD transitions. At low temperature the $^1E_u$ excited state is predicted to be electric dipole allowed in $x,y$ polarization and have a negative $A_1$ term MCD intensity. The $^3B_{2u}$ and $^3A_{1u}$ excited states will gain $x,y$ polarization and $-A_1$ and $+A_1$ term MCD intensity through spin–orbit coupling. Likewise, the $^3A_{1u}$ and $^3E_u(\Gamma_1^-,\Gamma_2^-)$ excited states will gain $z$ polarized intensity through spin–orbit coupling. All singlet states will be come allowed through vibronic coupling except the $^1A_{1u}$ excited state in $z$ polarization. As the temperature is raised, transitions from the thermally populated $^3A_{2u}$ ground state become allowed and are listed in Table II, columns 9 and 10. At higher temperatures the $^3E_g(\Gamma_1^+,\Gamma_2^+)$ and $^3E_g(\Gamma_3^+,\Gamma_4^+)$ excited states will have electric dipole allowed $+C_0$ and $-C_0$ term MCD (pseudo $A_1$) intensity, respectively. Spin–orbit coupling will allow the $^3B_{1g}$ and $^1B_{1g}$ excited states to gain negative $C_0$ term MCD intensity and $^3A_{2g}$ and $^1A_{2g}$ to gain positive $C_0$ term MCD intensity.

**Band Assignments.** The low-temperature $x,y$ polarized absorption spectrum has three bands (I, E, A) that correlate with the low-temperature MCD $A_1$ terms in Figure 5. The intense $x,y$ polarized band (I) with the negative MCD $A_1$ term at 15 475 cm$^{-1}$ is clearly the $^1A_{1g} \rightarrow {}^1E_u$ electric dipole allowed transition. Band E at 12 050 cm$^{-1}$ is assigned as the spin–orbit allowed $^1A_{1g} \rightarrow {}^3A_{1u}$ transition based upon its the positive MCD $A_1$ term and lower intensity. Band A is $x,y$ polarized and exhibits a negative MCD $A_1$ term at 10 000 cm$^{-1}$ and thus is assigned as the $^1A_{1g} \rightarrow {}^3B_{2u}$ spin–orbit allowed transition. The $A_1$ terms have skewed derivative band shapes due to the presence of magnetic field induced $B_0$ terms at the same energy.

The low-temperature $z$ polarized absorption spectrum in Figure 2 contains three ligand field bands designated H, C, and B. Figure 4 shows that band H is temperature independent, thus gaining its intensity (electric dipole) from spin–orbit coupling, whereas bands C and B exhibit an increase in intensity with temperature, indicating vibronic coupling. The selection rules in Table II predict two $z$ polarized spin–orbit allowed transitions. However, the $^3A_{1u}$ excited state has already been assigned in the $x,y$ polarized spectrum to be at 12 050 cm$^{-1}$, allowing the assignment of band H as the transition to the $\Gamma_2^-$ component of the $^3E_u$ excited state. As shown in Table II, there are five different excited states that are allowed to gain $z$ polarized intensity through vibronic coupling. The $^1E_u$ excited state has already been assigned at 15 475 cm$^{-1}$ and can be excluded as an assignment for bands B and C. The $^1E_g$ excited state should lie at comparably high energy and can also be excluded. Band C at 11 900 cm$^{-1}$ lies close in energy to the previously assigned $d_{xy}$ $^3A_{1u}$ and reasonably arises from a $d_{xy}$ derived excited state. Only one $d_{xy}$ excited state is predicted to have $z$ polarized vibronic intensity[29] allowing the assignment of band C at 11 900 cm$^{-1}$ as the $^1A_{2g}$ excited state. Two dimer $d_{z^2}$ excited states are predicted to have $z$ polarized vibronic intensity arising from $b_{2u}$ and $b_{1g}$ dimer vibrational modes. These vibrational modes correspond to symmetric and antisymmetric combinations of single-site vibrations and thus should induce equal intensity into the $^1B_{2u}$ and $^1B_{1g}$ excited states, respectively.[30] Band B at 10 500 cm$^{-1}$ can then be considered to derive from equal, overlapping contributions from both the $^1B_{2u}$ and $^1B_{1g}$ excited states, which are split in energy by less than 50 cm$^{-1}$.

The MCD spectrum associated with the $^3A_{2u}$ component of the ground state in Figure 6B contains three resolvable Gaussian bands

(29) It is intersting to note that the $d_{xy}$ excited state of the monomeric fragment does not have a single-site distortional mode that will allow intensity in the $z$ polarization. The $a_{1u}$ vibrational normal mode, which makes this transition allowed in the dimer, corresponds to a Cu–Cu torsion twist and is a true dimer vibration rather than a combination of single-site vibrational normal modes.

(30) The intensity observed in the $z$ polarization in the $d_{z^2}$ region of the copper acetate dimer is similar in magnitude to that observed in the square-planar $CuCl_4^{2-}$ monomer, indicating that the intensity originates from a single-site vibrational mechanism: Hitchman, M. A.; Cassidy, P. J. *Inorg. Chem.* **1979**, *18*, 1745–1754.

**Scheme I**

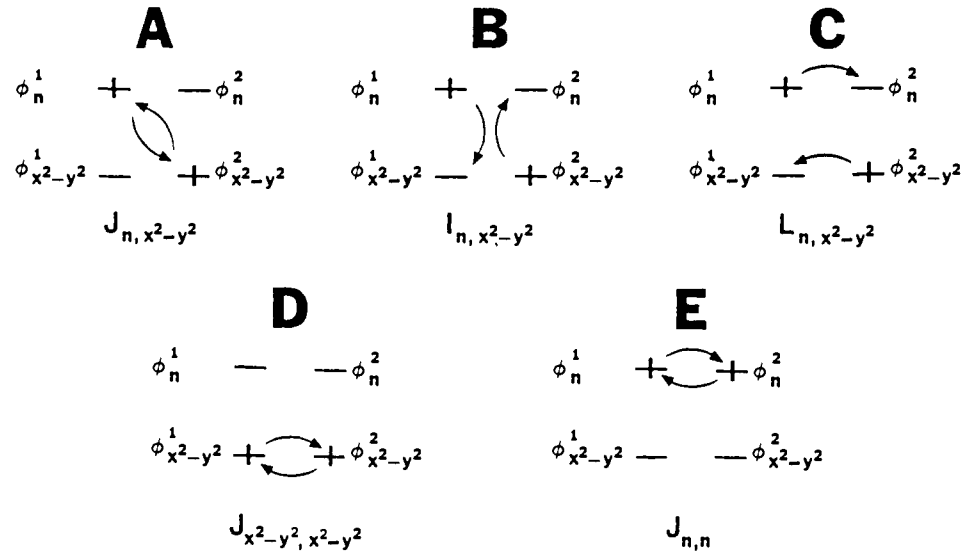


**Table III.** Band Properties and Assignments

| band | low-temp abs | low-temp MCD | high-temp MCD | energy, $cm^{-1}$ | assignment |
|---|---|---|---|---|---|
| A | $X,Y$ (s.o.) | $-A_1$ | | 10000 | $(z^2)\ ^3B_{2u}$ |
| B | $Z$ (vib) | | | 10500 | $(z^2)\ ^1B_{1g}$ and $^1B_{2u}$ |
| C | $Z$ (vib) | | $+C_0$ | 11900 | $(xy)\ ^1A_{2g}$ |
| D | | | $+C_0$ | 11950[a] | $(xy)\ ^3A_{2g}$ |
| E | $X,Y$ (s.o.) | $+A_1$ | | 12050 | $(xy)\ ^3A_{1u}$ |
| F | | | $+C_0$ | 14275[a] | $(xz,yz)\ ^3E_g\ \Gamma_1^+\ \Gamma_2^+$ |
| G | | | $-C_0$ | 14975[a] | $(xz,yz)\ ^3E_g\ \Gamma_3^+\ \Gamma_4^+$ |
| H | $Z$ | | | 15050 | $(xz,yz)\ ^3E_u\ \Gamma_1^-\ \Gamma_2^-$ |
| I | $X,Y$ (E dip.) | $-A_1$ | | 15475 | $(xz,yz)\ ^1E_u$ |

[a] Corrected for $^3A_{2u}$ ground state by adding 325 $cm^{-1}$.

(D, F, G). The dominant "pseudo" $A_1$ term at 14000 $cm^{-1}$ is composed of two overlapping opposite signed $C_0$ terms from the in-state spin–orbit split components of the $^3E_g$. The negative $C_0$ term to higher energy (G at 14975 $cm^{-1}$) is assigned (Table II, column 9) as the $^3E_g(\Gamma_3^+,\Gamma_4^+)$ and the lower energy positive $C_0$ term (F at 14275 $cm^{-1}$) is assigned as the $^3E_g(\Gamma_1^+,\Gamma_2^+)$. Based upon the in-state spin–orbit energy corrections in Figure 8 column C, the 700 $cm^{-1}$ splitting between these two spin–orbit components gives an experimental evaluation of the spin–orbit constant $\xi$ in eq 3 for this excited state. The free ion value is 830 $cm^{-1}$, indicating that orbital angular momentum has been reduced due to covalency. To lower energy only one positive $C_0$ term is resolvable (D at 11925 $cm^{-1}$), and no noticeable negative intensity is present. Group theory predicts two positive and two negative $C_0$ terms to lower energy. The two positive $C_0$ terms come from the $m_s = 0$ components of the $^1A_{2g}$ and $^3A_{2g}$ $d_{xy}$ excited states, which spin–orbit couple to the $^3E_g(\Gamma_1^+,\Gamma_2^+)$ state. These two states should have equal MCD intensities based upon their spin–orbit matrix elements (see Supplementary Material, Table S1). However, the $^1A_{2g}$ is also allowed in $z$ polarization due to vibronic coupling and has been assigned at 11900 $cm^{-1}$. The positive $C_0$ term (band D) at 11925 $cm^{-1}$ can thus be assigned as deriving from overlapping contributions from both the $^1A_{2g}$ and $^3A_{2g}$ excited states, and the energy of the $^3A_{2g}$ can be estimated at 11950 $cm^{-1}$. Note that the negative $C_0$ terms from the $^1B_{1g}$ and $^3B_{1g}$ states are predicted to be at lower energy but due to increased noise and lower PMT sensitivity they were not observed.

A total of 10 ligand field transitions (nine bands) have been assigned and are summarized in Table III. The excited-state spectrum can be divided into three energy regions with the $d_{xz,yz}$ states at highest energy, the $d_{xy}$ states next, and the $d_{z^2}$ states at lowest energy. Three components of each of the $d_{xy}$ and $d_{z^2}$ excited states have been assigned, and based upon the splitting pattern of these states, a direct evaluation of the excited-state singlet–triplet splitting, and the resonance (g–u) splitting (vide infra) can be obtained. Likewise, four components of the $d_{xz,yz}$ excited states have been assigned, allowing the additional evaluation of the spin–orbit coupling constant, $\xi$.

**Excited-State Exchange and Resonance Splittings.** Each monomer ligand field excited state corresponds to four dimer singly excited states due to symmetric and antisymmetric combinations of the spin and orbital portions of the wave function. The four dimer wave functions for an excitation of an electron from a general orbital, $d_n$, on a cupric ion to the $d_{x^2-y^2}$ orbital on the same ion are

$$^1\Phi_g = \tfrac{1}{2}[|\phi_n^1\bar{\phi}_{x^2-y^2}^2| - |\bar{\phi}_n^1\phi_{x^2-y^2}^2| + |\phi_{x^2-y^2}^1\bar{\phi}_n^2| - |\bar{\phi}_{x^2-y^2}^1\phi_n^2|] \quad (8a)$$

$$^1\Phi_u = \tfrac{1}{2}[|\phi_n^1\bar{\phi}_{x^2-y^2}^2| - |\bar{\phi}_n^1\phi_{x^2-y^2}^2| - |\phi_{x^2-y^2}^1\bar{\phi}_n^2| + |\bar{\phi}_{x^2-y^2}^1\phi_n^2|] \quad (8b)$$

$$^3\Phi_g = \tfrac{1}{2}[|\phi_n^1\bar{\phi}_{x^2-y^2}^2| + |\bar{\phi}_n^1\phi_{x^2-y^2}^2| - |\phi_{x^2-y^2}^1\bar{\phi}_n^2| - |\bar{\phi}_{x^2-y^2}^1\phi_n^2|] \quad (8c)$$

$$^3\Phi_u = \tfrac{1}{2}[|\phi_n^1\bar{\phi}_{x^2-y^2}^2| + |\bar{\phi}_n^1\phi_{x^2-y^2}^2| + |\phi_{x^2-y^2}^1\bar{\phi}_n^2| + |\bar{\phi}_{x^2-y^2}^1\phi_n^2|] \quad (8d)$$

Specific wave functions for each single ion d–d excitation have already been given in Table IB. From group theory these states are diagonal in $\mathbf{H}_{dimer}$, the total molecular Hamiltonian. Evaluation of $\mathbf{H}_{dimer}$ over these wave functions leads to the energy expressions eq 9a–d, which produce the splitting pattern given in Figure 9.

$$E(^1\Phi_g) = K_{n,x^2-y^2} + J_{n,x^2-y^2} + I_{n,x^2-y^2} + L_{n,x^2-y^2} \quad (9a)$$

$$E(^1\Phi_u) = K_{n,x^2-y^2} + J_{n,x^2-y^2} - I_{n,x^2-y^2} - L_{n,x^2-y^2} \quad (9b)$$

$$E(^3\Phi_g) = K_{n,x^2-y^2} - J_{n,x^2-y^2} - I_{n,x^2-y^2} + L_{n,x^2-y^2} \quad (9c)$$

$$E(^3\Phi_u) = K_{n,x^2-y^2} - J_{n,x^2-y^2} + I_{n,x^2-y^2} - L_{n,x^2-y^2} \quad (9d)$$

These energy splittings are given in terms of the four matrix elements defined below.

$$K_{n,x^2-y^2} = \langle\phi_n^1(1)\phi_{x^2-y^2}^2(2)|\mathbf{H}_{dimer}|\phi_n^1(1)\phi_{x^2-y^2}^2(2)\rangle \quad (10a)$$

$$J_{n,x^2-y^2} = \langle\phi_n^1(1)\phi_{x^2-y^2}^2(2)|\mathbf{H}_{dimer}|\phi_n^1(2)\phi_{x^2-y^2}^2(1)\rangle \quad (10b)$$

$$I_{n,x^2-y^2} = \langle\phi_n^1(1)\phi_{x^2-y^2}^2(2)|\mathbf{H}_{dimer}|\phi_{x^2-y^2}^1(1)\phi_n^2(2)\rangle \quad (10c)$$

$$L_{n,x^2-y^2} = \langle\phi_n^1(1)\phi_{x^2-y^2}^2(2)|\mathbf{H}_{dimer}|\phi_{x^2-y^2}^1(2)\phi_n^2(1)\rangle \quad (10d)$$

$K_{n,x^2-y^2}$ and $J_{n,x^2-y^2}$ are Coulomb and exchange terms between an excited state on copper 1 and a ground state on copper 2, while, $I_{n,x^2-y^2}$ and $L_{n,x^2-y^2}$ correspond to an excitation transfer of an excited state from copper 1 to copper 2 mediated through Coulomb and exchange interactions, respectively.

The Coulomb matrix element $K_{n,x^2-y^2}$ has contributions from both one- and two-electron operators and adds equally to all four states producing an average energy increase of these states as shown in Figure 9. The exchange term, $J_{n,x^2-y^2}$, produces a splitting of the singlet and triplet components of a given excited state by

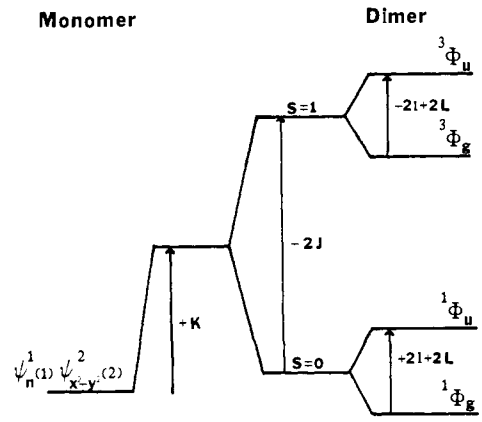


**Figure 9.** Monomer to dimer excited-state splitting diagram. The Coulomb interaction (K) represents an average energy shift from the monomer to the dimer. The exchange interaction ($J$) splits the excited state into singlet and triplet states. The excitation transfer interactions ($I$ and $L$) split the singlets and triplets into g–u resonance components.

$-2J_{n,x^2-y^2}$. This $J_{n,x^2-y^2}$ exchange pathway is schematically shown in Scheme IA. In comparison to the ground-state $J_{x^2-y,x^2-y^2}$ pathway in Scheme ID, $J_{n,x^2-y^2}$ involves new superexchange pathways between $d_{x^2-y^2}$ and $d_n$ orbitals. Thus, the value of $J_{n,x^2-y^2}$ can differ from that of the ground state and can be different for each excited state, n.

The third term, $I_{n,x^2-y^2}$, corresponds to an excitation transfer mediated through a Coulomb interaction.[31] This is diagrammed in Scheme IB. Note that this term involves deexcitation of copper 1 with a simultaneous excitation of copper 2. Therefore, this excitation transfer interaction can then be estimated by a dipole–dipole approximation:[31,32]

$$I_{n,x^2-y^2} = -1.162 \times 10^5 |M|^2 \{3\cos^2\theta - \cos\phi\}/R^3 \quad (11)$$

where $M$ is the transition dipole moment (given in Å), $R$ is the distance between transition dipoles (in Å), $\theta$ is the angle between the dipole and the **R** vector, and $\phi$ is the angle between the dipoles. The value of $M$ can be obtained from the intensity of an absorption band, while $\theta$ and $\phi$ are defined by the polarization behavior of the absorption band. When $I_{n,x^2-y^2}$ is calculated from eq 11 for the $d_{xy}$ or $d_{z^2}$ excited states, a value of $I_{n,x^2-y^2} = 3$ cm$^{-1}$ is obtained. As the transition to the $d_{xz,yz}$ excited state is more intense ($f \simeq 6.5 \times 10^{-4} = M^2 \simeq 4 \times 10^{-3}$ Å$^2$), the magnitude of $I_{n,x^2-y^2}$ is somewhat larger, having a value of $I_{xzyz,x^2-y^2} = 25$ cm$^{-1}$ ($x,y$ polarized, $\theta = 90°$, $\phi = 0°$).

The matrix element $L_{n,x^2-y^2}$ corresponds to an exchange-mediated excitation transfer[31,33] as shown in Scheme IC. It its important to note that the electrons change centers while also transferring the excitation, whereas the $I_{n,x^2-y^2}$ term in Scheme IB did not involve exchange of electrons between metal centers. A combination of the exchange- and Coulomb-mediated excitation transfer terms leads to a g–u splitting of the singlet and triplet components as given in eq 9a–d and shown in Figure 9.

The experimental transition energies listed in Table III and the energy splittings defined in eq 6a–d and Figure 9 have been used to obtain estimates of the parameters associated with the singlet–triplet and g–u splittings for each d–d transition, and these have been tabulated in Table IV. For the $d_{xy}$ excited state the energy difference between the $^1A_{2g}$ at 11 900 cm$^{-1}$ and the $^3A_{2g}$ at 11 950 cm$^{-1}$ is 50 cm$^{-1}$. As the calculated value of $I_{xy,x^2-y^2}$ is negligible, $-2J_{xy,x^2-y^2}$ can be estimated as a 50 cm$^{-1}$ antiferromagnetic interaction. Likewise, the 100 cm$^{-1}$ difference between the $^3A_{2g}$ and $^3A_{1u}$ states is equal to $-2L_{xy,x^2-y^2}$. Using the four assigned components of the $d_{xz,yz}$ excited state listed in Table III with measured spin–orbit splitting of 700 cm$^{-1}$ and the value for $I_{xzyz,x^2-y^2}$ of 25 cm$^{-1}$ gives values of −125 cm$^{-1}$ for $-2J_{xzyz,x^2-y^2}$ and 725 cm$^{-1}$ for $-2L_{xzyz,x^2-y^2}$. The $^1B_{2u}$ and $^1B_{1g}$ components of the $d_{z^2}$ to $d_{x^2-y^2}$ single-center excitation are approximately equal in energy, thus $-2L_{z^2,x^2-y^2}$ is small, and $-2J_{z^2,x^2-y^2}$ is a large ferromagnetic interaction of approximately −500 cm$^{-1}$. This provides an ordering of $-2J_{n,x^2-y^2}$ for the different ligand field states:

$$-2J_{x^2-y,x^2-y^2} > -2J_{xy,x^2-y^2} > -2J_{xzyz,x^2-y^2} > -2J_{z^2,x^2-y^2}$$

It is important to note that the excited-state values are different from the ground state and are observed to vary from ferromagnetic for $d_{z^2}$ and $d_{xz,yx}$ to antiferromagnetic for $d_{xy}$. Likewise, the ordering of $-2L_{n,x^2-y^2}$ for the different ligand field states is

$$-2L_{xzyz,x^2-y^2} > -2L_{xy,x^2-y^2} > -2L_{z^2,x^2-y^2}$$

These values are all positive having the even parity state to lowest energy, and the $d_{xz,yz}$ excited state having the largest g–u splitting.

Further insight into the physical origin of $-2L_{n,x^2-y^2}$ may be obtained from a consideration of the superexchange pathways presented in Scheme IC–E. As noted earlier, $L_{n,x^2-y^2}$ involves excitation transfer by electron exchange between metal centers. As illustrated in Scheme IC the $L_{n,x^2-y^2}$ interaction proceeds via a superexchange pathway connecting the two excited states on each metal and also through a pathway connecting the two ground states. The orbital pathway for the excitation exchange in $L_{n,x^2-y^2}$ (Scheme IC) can then be decomposed into a combination of the ground-state orbital pathway of $J_{x^2-y^2,x^2-y^2}$ (Scheme ID) and a doubly excited state orbital pathway of $J_{n,n}$ (Scheme IE). By expanding the total dimer Hamiltonian into one- and two-electron operators and applying the Wolfberg–Helmholtz approximation,[34] a relationship (eq 12)

$$L_{n,x^2-y^2} \simeq (J_{x^2-y,x^2-y^2} \cdot J_{n,n})^{1/2} \quad (12)$$

(31) Craig, D. P.; Walmsley, S. H. *Excitons in Molecular Crystals*; Benjamin: New York, 1968.
(32) Kasha, M.; Rawls, H. R.; El-Bayoumi, M. A. *Pure Appl. Chem.* **1965**, *11*, 371–392.
(33) Tanabe, Y.; Aoyagi, K. In *Excitons*; Rashba, E. I., Sturge, M. D., Eds.; North-Holland: Amsterdam, The Netherlands, 1982; pp 603–663.

(34) Considering only one-electron contributions to the dimer Hamiltonian

$$\mathbf{H}_{dimer} = h(1) + h(2) \quad (a)$$

gives

$$L_{n,x^2-y^2} = \langle\phi^1_n(1)|h(1)|\phi^2_n(1)\rangle\langle\phi^2_{x^2-y^2}(2)|\phi^1_{x^2-y^2}(2)\rangle + \langle\phi^1_n(1)|\phi^2_n(1)\rangle\langle\phi^2_{x^2-y^2}(2)|h(2)|\phi^1_{x^2-y^2}(2)\rangle \quad (b)$$

Defining

$$\alpha_n = \langle\phi^1_n(1)|h(1)|\phi^1_n(1)\rangle$$

$$\alpha_{x^2-y^2} = \langle\phi^1_{x^2-y^2}(2)|h(2)|\phi^1_{x^2-y^2}(2)\rangle$$

$$S_n = \langle\phi^1_n(1)|\phi^2_n(1)\rangle$$

$$S_{x^2-y^2} = \langle\phi^1_{x^2-y^2}(2)|\phi^2_{x^2-y^2}(2)\rangle$$

$$\beta_n = \langle\phi^1_n(1)|h(1)|\phi^2_n(1)\rangle$$

$$\beta_{x^2-y^2} = \langle\phi^1_{x^2-y^2}(1)|h(1)|\phi^2_{x^2-y^2}(1)\rangle$$

and make the Wolfberg–Helmholtz approximation

$$\beta_n = k_n\alpha_n S_n$$

$$\beta_{x^2-y^2} = k_{x^2-y^2}\alpha_{x^2-y^2}S_{x^2-y^2}$$

gives

$$\begin{aligned} L_{n,x^2-y^2} &= \beta_n S_{x^2-y^2} + \beta_{x^2-y^2}S_n \\ &= k_n\alpha_n S_n S_{x^2-y^2} + k_{x^2-y^2}\alpha_{x^2-y^2}S_{x^2-y^2}S_n \\ &= 2S_n S_{x^2-y^2}(k_n\alpha_n + k_{x^2-y^2}\alpha_{x^2-y^2})/2 \end{aligned} \quad (c)$$

Similarly,

$$J_{x^2-y,x^2-y^2} = 2S^2_{x^2-y^2}k_{x^2-y^2}\alpha_{x^2-y^2}$$

$$J_{n,n} = 2S^2_n k_n\alpha_n \quad (d)$$

Using the approximation

$$(k_n\alpha_n + k_{x^2-y^2}\alpha_{x^2-y^2})/2 \simeq (k_n\alpha_n k_{x^2-y^2}\alpha_{x^2-y^2})^{1/2}$$

gives

$$L_{n,x^2-y^2} \simeq 2S_n S_{x^2-y^2}(k_n\alpha_n k_{x^2-y^2}\alpha_{x^2-y^2})^{1/2} \quad (e)$$

substitution of eq d gives $L_{n,x^2-y^2} \simeq (J_{x^2-y,x^2-y^2} \cdot J_{n,n})^{1/2}$. It can also be shown that inclusion of two electron terms in eq a does not change this final expression due to their cancellation.

Table IV. Exchange Interactions between Pairs of $d_n$ Orbitals

| n | $-2J_{n,x^2-y^2}$ | $-2L_{n,x^2-y^2}$ | $-2J_{n,n}$ |
|---|---|---|---|
| $x^2-y^2$ | | | 325 |
| $xy$ | 50 | 100 | 31 |
| $xz,yz$ | −125 | 725 | 1617 |
| $z^2$ | −250 | <50 | <8 |

between these interactions can be obtained that allows an estimate of the magnitude of $J_{n,n}$ from the experimental values of the excited-state $L_{n,x^2-y^2}$ and the ground-state $J_{x^2-y,x^2-y^2}$. Thus, knowledge of the singly excited resonance splittings and the ground-state exchange splitting can provide quantitative insight into the exchange interactions between the doubly excited state metal orbitals. $J_{n,n}$ have been estimated for all excited states by using eq 12 and are included in Table IV. The ordering of $J_{n,n}$ must parallel that of $L_{n,x^2-y^2}$:

$$-2J_{xzyz,xzyz} > -2J_{x^2-y^2,x^2-y^2} > -2J_{xy,xy} > -2J_{z^2,z^2}$$

An unexpected feature is the larger magnitude of $J_{xzyz,xzyz}$ in relation to the ground-state $J_{x^2-y^2,x^2-y^2}$.

**$^3A_{1u}$ Excited-State Spin Hamiltonian Parameters.** The Zeeman interaction on the structured origin of band E (Figure 7) splits the origin into two peaks when the light is polarized perpendicular to the magnetic field, but the origin remains as one peak when the light is polarized parallel to the magnetic field. This polarization behavior is consistent with a triplet excited state. When the magnetic field lies along the molecular $z$ direction, the symmetry of the dimer is reduced to $C_{4h}'$, with the $m_s = 0$ spin component of a triplet transforming as $\Gamma_1^+$ and therefore $z$ polarized, while the $m_s = \pm 1$ spin components, which transform as $\Gamma_3^+$ and $\Gamma_4^+$, are polarized along $x$ and $y$ directions. However, band E has no intensity in the $z$ polarization and the $m_s = 0$ spin component is not observed. When the magnetic field is along the molecular $x$ or $y$ direction, the symmetry of the dimer is reduced to $C_{2h}'$. The $m_s = 0$ spin component transforms as $\Gamma_1^+$ and is polarized along the magnetic field direction, while the $m_s = \pm 1$ spin components transform as $\Gamma_2^+$ and are polarized perpendicular to the magnetic field. Therefore the $m_s = 0$ spin component is assigned as the field independent band polarized parallel to the magnetic field directions in Figure 7B ($\mathbf{H}\|x$) and C ($\mathbf{H}\|y$). The $m_s = \pm 1$ spin components are assigned as the bands polarized perpendicular to the magnetic field as seen in Figure 7B ($\mathbf{H}\|z,y$) and C ($\mathbf{H}\|z,x$).

The field dependence of the energies is described by the triplet spin Hamiltonian[35] (eq 13):

$$\mathbf{H} = \beta[g_x S_x \vec{H}_x + g_y S_y \vec{H}_y + g_z S_z \vec{H}_z] + D[S_z^2 - \tfrac{2}{3}] + E[S_x^2 - S_y^2] \quad (13)$$

where the energies of the spin components are given by the following expressions for each magnetic field direction.

$\mathbf{H}\|z$

$$\epsilon = \tfrac{1}{3}D \pm (g_z^2\beta^2H^2 + E^2)^{1/2} \quad (14a)$$

$$\epsilon = -\tfrac{2}{3}D \quad (14b)$$

$\mathbf{H}\|x$

$$\epsilon = -\tfrac{1}{6}D + \tfrac{1}{2}E \pm [g_x^2\beta^2H^2 + \tfrac{1}{4}(D+E)^2]^{1/2} \quad (14c)$$

$$\epsilon = \tfrac{1}{3}D - E \quad (14d)$$

$\mathbf{H}\|y$

$$\epsilon = -\tfrac{1}{6}D - \tfrac{1}{2}E \pm [g_y^2\beta^2H^2 + \tfrac{1}{4}(D-E)^2]^{1/2} \quad (14e)$$

$$\epsilon = \tfrac{1}{3}D + E \quad (14f)$$

A best fit to the field dependence of the experimental energies of the Zeeman split spin components, shown as circles in Figure 7D, was achieved with the excited-state spin Hamiltonian parameters: $g_x = 2.12$, $g_y = 2.23$, $g_z = 1.42$, $D = 6.0$ cm$^{-1}$, and $E = 0.3$ cm$^{-1}$. The fit calculated from these parameters is given as the solid line in Figure 7D.

The intensities of the spin components will also show a field-dependent nature due to magnetic field induced mixing of the zero-field spin states. When the magnetic field is parallel to the $z$ molecular axis, the intensities of the spin states are constant with increasing magnetic field strength, consistent with the fact that the zero-field spin states are diagonal along $z$. However, when the magnetic field is along the $x$ or $y$ direction, the zero-field spin states will mix as a function of the magnetic field strength, producing unequal intensities in the "$m_s \pm 1$" spin states. The spin Hamiltonian parameters for the $^3A_{1u}$ excited state given above were used to generate the field-dependent spin wave functions of the form

$$|\psi_i\rangle = C_i^{+1}|m_s = +1\rangle + C_i^{0}|m_s = 0\rangle + C_i^{-1}|m_s = -1\rangle \quad (15)$$

where the zero-field spin states form a basis set with $C_i^{\pm 1,0}$ being the field-dependent coefficient. The $x,y$ polarized intensity of the field-dependent wave functions is given by

$$I_i(\mathbf{H}) = [(C_i^{+1})^2 + (C_i^{-1})^2]I_{\pm 1}(0) \quad (16)$$

where $I_i(\mathbf{H})$ is the field-dependent intensity of the $i$th spin component and $I_{\pm 1}(0)$ is the intensity of the $m_s = \pm 1$ spin component at zero field. The calculated intensities are shown as solid lines in Figure 7E,F. When a small magnetic field is applied along the $x(y)$ molecular direction, the "$m_s = +1$" spin component that shifts to higher energy is mainly composed of the zero-field $m_s = 0$ ($z$ polarized) spin state. Although having almost no intensity at small fields, the "$m_s = +1$" spin state will increase in intensity at higher fields due to gaining increased zero-field $m_s = \pm 1$ ($x,y$ polarized) spin-state character. A corresponding decrease in intensity occurs in the "$m_s = 0$" spin component as it gains zero-field $m_s = 0$ ($z$ polarized) spin character at higher fields.

The deviation of the $g$ values from the 2.00 spin-only value is due to spin–orbit coupling between the d orbitals. An expression for the second-order corrected $g$ values is

$$g_i = 2.00 + \lambda_{\text{dimer}} \sum_{i,j,e} \frac{\langle\psi_e|\mathbf{L}_{i,j}|\psi_e\rangle\langle\psi_e|\mathbf{L}_{i,j}|\psi_{e'}\rangle}{E_{e'} - E_e} \quad (17)$$

where $\mathbf{L}_{i,j}$ is the orbital angular momentum operator for $i = x, y, z$ on center $j$, $\lambda_{\text{dimer}}$ equals $-\xi/2$, and e′ refers to the state for which the $g$ value is being calculated. From this expression, estimates of the $g$ values for the triplet excited states may be obtained. In-state spin–orbit coupling will split each of the $^3E_g$ and $^3E_u$ excited states into three sets of doubly degenerate states, (Figure 8C,D). Hence these spin–orbit coupled states will not exhibit the characteristic triplet splitting pattern described by the spin Hamiltonian (eq 13). Using the experimentally derived values for $\lambda_{\text{dimer}}$, the excited-state energies, and eq 17, the $g$ values for the spin triplet d–d dimer excited states can be calculated. The $^3B_{1g'}$ and $^3B_{2u}$ excited states are predicted to have $g_z = 2.00$, $g_{x,y} = 2.56$, the $^3A_{2g}$ should have $g_z = 2.00$, $g_{x,y} = 2.32$, and the $^3A_{1u}$ excited state should have $g_z = 1.65$, $g_{x,y} = 2.32$. The orbital angular momentum operator transforms with even parity and will not mix even parity excited states with the ground-state triplet, which has odd parity. Therefore, the only excited state capable of having a $g_z$ value less than 2.00 is the $^3\Phi_3(A_{1u})$ excited state, which is an excitation from the $d_{xy}$ orbital and couples to the ground-state triplet via $L_z$. This strongly supports the previous assignment of band E (Table III). It is important to note that the **D** value of 6.0 cm$^{-1}$ for the $^3A_{1u}$ is much larger than the ground-state value of 0.33 cm$^{-1}$ and will be considered in detail in the next section.

**Anisotropic Exchange Contribution to Zero-Field Splitting.** Anisotropic exchange or pseudo-dipolar coupling has been widely used to explain the large ground-state triplet zero-field splitting in copper dimers.[1,6,36] The normal dipolar contribution to the

(35) McGarvey, B. R. In *Transition Metal Chemistry*; Carlin, R. L., Ed.; Marcel-Dekker: New York, 1967; Vol. 3, pp 89–201.

(36) For example: (a) Banci, L.; Bencini, A.; Gatteschi, D. *J. Am. Chem. Soc.* **1983**, *105*, 761–764. (b) Bencini, A.; Gatteschi, D.; Zanchini, C. *Inorg. Chem.* **1986**, *25*, 2211–2214.

ground-state zero-field splitting can be estimated from the distance between metal centers as given in eq 18.[37] The dipolar contribution to zero-field splitting is smaller in magnitude ($-0.12$ cm$^{-1}$)[7] and of opposite sign than the experimental ground-state zero-field splitting of 0.33 cm$^{-1}$ in copper acetate. Anisotropic exchange involves a third-order perturbation mechanism of spin–orbit coupling to an excited state in second order plus an excited-state exchange interaction as given in eq 19.[7]

$$D^{dip} = -(2g_{\parallel}^2 + g_{\perp}^2)\beta^2/2r^3 \quad (18)$$

$$\mathbf{H} = \langle g_1g_2|\xi\mathbf{L}_1\cdot\mathbf{S}_1|e_1g_2\rangle\langle e_1g_2|H_{ex}|e_1g_2\rangle\langle e_1g_2|\xi\mathbf{L}_1\cdot\mathbf{S}_1|g_1g_2\rangle/(E_e - E_g)^2 \quad (19)$$

where $g_i$ and $e_i$ represent the ground and excited states on center $i$, $\xi\mathbf{L}_i\cdot\mathbf{S}_i$ is the spin–orbit operator on center $i$, and $H_{ex}$ is the excited-state exchange interaction. By writing $H_{ex}$ as $-2J\mathbf{S}_1\cdot\mathbf{S}_2$ and expanding the interaction with effective axial symmetry, the interaction can be written in the usual dipolar form

$$\mathbf{H} = D^{ex}(3S_{1z}S_{2z} - \mathbf{S}_1\cdot\mathbf{S}_2) \quad (20)$$

where the anisotropic exchange contribution to the ground-state zero-field splitting in copper acetate is given as

$$D^{ex}_{x^2-y^2} = -\tfrac{1}{16}(g^{gs}_{\parallel} - 2)^2J_{xy,x^2-y^2} + \tfrac{1}{4}(g^{gs}_{\perp} - 2)^2J_{xzyz,x^2-y^2} \quad (21)$$

In the past, the difficulty in analyzing this contribution has been in having no experimental value for the excited-state exchange interaction $J_{xy,x^2-y^2}$ and therefore having to estimate it from theory. As we have now directly measured the excited-state exchange interactions $J_{xy,x^2-y^2}$ and $J_{xzyz,x^2-y^2}$ (Table IV) and as the ground-state $g$ values are known ($g_{\parallel} = 2.350$, $g_{\perp} = 2.064$), a value of **D** can be calculated from eq 21. The calculated value for the total (including dipolar) ground-state zero-field splitting $D_{x^2-y^2} = 0.14$ cm$^{-1}$ is of the correct sign and magnitude, but smaller than the experimental value of 0.33 cm$^{-1}$. Note that the $g_{\perp}$ term is usually neglected, whereas we find this actually contributes 0.06 cm$^{-1}$.

The same mechanism can be further considered for excited-state zero-field splitting parameters. The perturbation expression for the excited-state interaction is given by eq 22,

$$\mathbf{H} = \langle e_1g_2|\xi\mathbf{L}_1\cdot\mathbf{S}_1|e_1'g_2\rangle\langle e_1'g_2|H_{ex}|e_1'g_2\rangle\langle e_1'g_2|\xi\mathbf{L}_1\cdot\mathbf{S}_1|e_1g_2\rangle/(E_{e'} - E_e)^2 \quad (22)$$

which involves spin–orbit coupling of an excited state to another state, $e'$, plus the exchange interaction of state $e'$ on one metal center with the ground state on the other metal center. The anisotropic exchange contribution to the $d_{xy}$ excited-state zero-field splitting in copper acetate involves spin–orbit coupling to the $d_{x^2-y^2}$ ground state. Equation 23

$$D^{ex}_{xy} = -\tfrac{1}{16}(g^{es}_{\parallel} - 2)^2J_{x^2-y^2,x^2-y^2} + \tfrac{1}{4}(g^{es}_{\perp} - 2)^2J_{x^2-y^2,xzyz} \quad (23)$$

therefore relates the $^3A_{1u}$ ($d_{xy}$) excited-state zero-field splitting to the ground-state exchange interaction $J_{x^2-y^2,x^2-y^2}$. The zero-field splitting of the $^3A_{1u}$ ($d_{xy}$) excited state has been found from the Zeeman experiments to have a value of $D_{xy} = 6.0$ cm$^{-1}$. Using the $g$ values determined for the $^3A_{1u}$ ($d_{xy}$) excited state and the ground-state $J_{x^2-y^2,x^2-y^2}$ value of 325 cm$^{-1}$, a value of $D_{xy} = 3.8$ cm$^{-1}$ is calculated that is in reasonable agreement with the experiment. This is the first time that eq 21 and 23 have been experimentally evaluated for copper dimers. The general agreement with the data indicates that anisotropic exchange is a reasonable model for the origin of zero-field splitting in copper dimers.

## Discussion

The present study generates an experimental assignment of the ligand field spectra of the copper acetate system using magneto-optical techniques. Key features of these experiments include the use of variable-temperature MCD to observe transitions originating from the triplet component of the ground state, and Zeeman interactions on the sharp vibronic structure of the $^3A_{1u}$ ($d_{xy}$) excited state to obtain spin Hamiltonian parameters. The combination of linearly polarized absorption, variable-temperature MCD, and Zeeman spectroscopies has allowed the assignment of 10 excited states and the direct evaluation of the energy splittings between the dimer components of each ligand field transition.

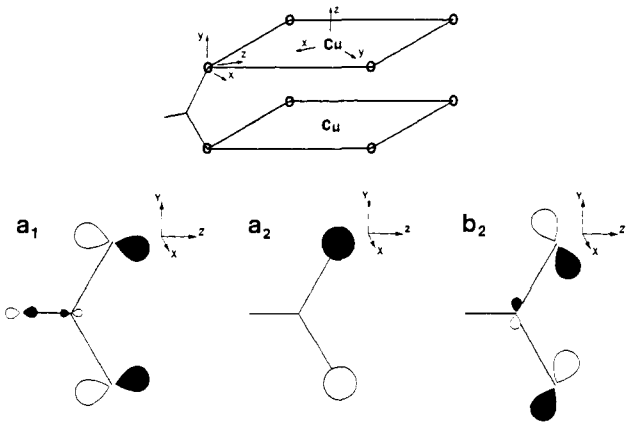


**Figure 10.** The acetate ion highest occupied nonbonding molecular orbitals in $C_{2v}$ symmetry.[13]

We have seen that each ligand field excited state, $d_n$, in a binuclear copper system will have four components due to symmetric and antisymmetric combinations of singlets and triplets. As summarized in Figure 9, the two singlet and two triplet excited states will be separated by an amount $-2J_{n,x^2-y^2}$ due to the exchange interaction between unpaired electrons in the ground and excited state. The singlets and triplets will each be further split due to Coulomb and exchange excitation transfer interactions, $I_{n,x^2-y^2}$ and $L_{n,x^2-y^2}$. On the basis of the knowledge of the transition dipole magnitude and orientation, the value of $I_{n,x^2-y^2}$ can be estimated from a dipole approximation. Furthermore, it has been shown that the value of $L_{n,x^2-y^2}$ can be directly related to the magnitude of $J_{x^2-y^2,x^2-y^2}$ and $J_{n,n}$, allowing an estimate of the value of $J_{n,n}$. The experimental evaluation of $J_{x^2-y^2,x^2-y^2}$ and $J_{n,x^2-y^2}$ and the estimation $J_{n,n}$ provides direct insight into the superexchange pathways between all the different combinations of d orbitals on each copper.

Past research in antiferromagnetically coupled transition-metal systems has produced a general understanding of the magnitude and sign of the ground-state exchange interaction.[4,5,8] The models and concepts developed for the ground state can now be extended to the excited-state interactions and compared to experimental values. The values of the exchange interactions between the ground and excited states, $J_{n,x^2-y^2}$, listed in Table IV range from weakly antiferromagnetic to strongly ferromagnetic. In comparison, the exchange interactions between similar magnetic orbitals, $J_{n,n}$, range from negligibly small to very large and are all antiferromagnetic. This wide range of values is the result of two competing contributions to the exchange interaction. The negative, antiferromagnetic term is directly related to the magnitude of the magnetic orbital overlap ($S_{n,x^2-y^2}$ or $S_{n,n}$).[5] Whereas, the positive, ferromagnetic contribution originates from the standard two-electron exchange integral, $j_{n,x^2-y^2}$ or $j_{n,n}$, and has been related to the density of the magnetic orbital overlap.[38] If the magnetic orbitals have areas of large overlap density, the ferromagnetic term will be large due to large spin repulsion in these regions.

Since $J_{n,x^2-y^2}$ involves orbitals that are orthogonal in the $D_{4h}$ effective symmetry of copper acetate, the antiferromagnetic term is initially expected to be zero. To evaluate the ferromagnetic contribution to $J_{n,x^2-y^2}$ one must consider delocalization of the $d_n$ orbital onto the bridging acetate ligand. The highest occupied orbitals of the acetate ion ($C_{2v}$ symmetry) are the nonbonding $a_1$,

(37) Abragam, A.; Bleaney, B. *Electron Paramagnetic Resonance on Transition Ions*; Clarendon Press: Oxford, 1970.

(38) (a) Kahn, O.; Charlot, M. F. *Nouv. J. Chim.* **1980**, *4*, 567–576. (b) Kahn, O. *J. Magn. Magn. Mater.* **1986**, 54–57, 1459–1463. (c) Charlot, M. F.; Journaux, Y.; Kahn, O.; Bencini, A.; Gatteschi, D.; Zanchini, C. *Inorg. Chem.* **1986**, *25*, 1060–1063.

**Table V.** Symmetry Representations of the Copper and Acetate Monomer Orbitals and the Corresponding Molecular Orbitals

| Copper Orbitals | |
|---|---|
| copper monomer ($C_{4v}$) | copper dimer ($D_{4h}$) |
| $x^2 - y^2$ ($b_1$) | $b_{1g}$, $b_{2u}$ |
| $z^2$ ($a_1$) | $a_{1g}$, $a_{2u}$ |
| $xy$ ($b_2$) | $b_{2g}$, $b_{1u}$ |
| $xz,yz$ (e) | $e_g$, $e_u$ |
| **Acetate Orbitals** | |
| acetate monomer ($C_{2v}$) | acetate tetramer ($D_{4h}$) |
| $P_z$ ($a_1$) | $a_{1g}$, $b_{2g}$, $e_u$ |
| $P_x$ ($a_2$) | $a_{1u}$, $b_{1u}$, $e_g$ |
| $P_y$ ($b_2$) | $a_{2u}$, $b_{2u}$, $e_g$ |

$a_2$, and $b_2$, which are predominantly composed of oxygen $2p_z$, $2p_x$, and $2p_y$ orbitals, respectively, as shown in Figure 10.[13] The $d_{x^2-y^2}$ orbital should have the largest amount of delocalization due to a strong $\sigma$-bonding interaction with the acetate $a_1$ orbital. The $d_{z^2}$ should also interact with the $a_1$ but will have a much poorer overlap. The $d_{xz,yz}$ orbital should form a fairly strong $\pi$-bonding interaction with the acetate $b_2$ and also overlap with the $a_1$ through a pseudo-$\sigma$ interaction. Finally, the $d_{xy}$ will have a $\pi$ interaction with the acetate $a_2$. The resultant magnetic orbitals that have the largest spin density in the same ligand orbitals will have the largest ferromagnetic term. The $d_{x^2-y^2}$ and $d_{z^2}$ orbitals each have significant spin density in the $a_1$ orbital and thus are expected to have a large ferromagnetic contribution to $J_{z^2,x^2-y^2}$. Similarly $J_{xzyz,x^2-y^2}$ will have a smaller positive value and $J_{xy,x^2-y^2}$ will have the smallest ferromagnetic contribution, in general agreement with Table IV.

The fact that $J_{xy,x^2-y^2}$ is experimentally found to be antiferromagnetic based both on the singlet–triplet splitting order and on the sign of $D_{x^2-y^2}$ requires further consideration of the antiferromagnetic contribution to $J_{n,x^2-y^2}$. As indicated above, in the $D_{4h}$ symmetry of the dimer the d orbitals are orthogonal, requiring all $J_{n,x^2-y^2}$ values to be positive due to a zero antiferromagnetic contribution. This symmetry-restricted orthogonality remains even in the crystallographic $C_s$ monomer site symmetry of copper acetate pyrazine; the $d_{x^2-y^2}$ orbital transforms as A″ while the other d orbitals transform as A′.[39] However, the inclusion of spin–orbit coupling will allow the ground state to mix with the $d_{xy}$ and $d_{xz,yz}$ excited states, producing a nonzero antiferromagnetic contribution to $J_{n,x^2-y^2}$. While spin–orbit mixing is relatively small ($\langle xy|l\cdot s|x^2-y^2\rangle^2/\Delta E \simeq 5\%$), this addition of the experimentally antiferromagnetic $J_{x^2-y^2,x^2-y^2}$ appears to be enough to overcome the small $j_{xy,x^2-y^2}$ term. However, spin–orbit mixing with $d_{xz,yz}$ is not large enough to overcome the larger $j_{xzyz,x^2-y^2}$ contribution, and since spin–orbit coupling does not occur in $d_{z^2}$, $J_{z^2,x^2-y^2}$ remains a large ferromagnetic interaction. In summary, the variation in the experimental values of $J_{n,x^2-y^2}$ appears to result from differences in ferromagnetic interactions that are modified due to the addition of a small antiferromagnetic contribution through the spin–orbit mixing.

In applying ground-state exchange concepts to the $J_{n,n}$ interaction, it is convenient to estimate the antiferromagnetic contribution by using the method of Hay, Thibeault, and Hoffmann, which relates to $J_{n,n}$ to the energy difference of the $d_n$ orbital derived molecular orbitals of the dimer.[4] As shown in Table V, the $d_{x^2-y^2}$ orbitals form $b_{1g}$ and $b_{2u}$ symmetry combinations in the dimer ($D_{4h}$ symmetry), which will interact with the acetate $a_1$ and $b_2$ orbitals, respectively, based on their dimer symmetry. Due to a good $\sigma$ interaction with the $a_1$ and a poor $\pi$ interaction with the $b_2$, the $b_{1g}$ and $b_{2u}$ molecular orbitals should have a large energy splitting and thus a large antiferromagnetic contribution to $J_{x^2-y^2,x^2-y^2}$. Similarly, the $d_{z^2}$ orbitals, which interact with the $a_1$ and $b_2$ acetate orbitals to form $a_{1g}$ and $a_{2u}$ dimer molecular orbitals, will have a small splitting due to poor overlap. The $d_{xz,yz}$ orbitals will overlap with the $b_2$ via a $\pi$ interaction to form a molecular oribtal with $e_g$ symmetry and with the $a_1$ orbital via a pseudo-$\sigma$ interaction forming a molecular orbital with $e_u$ symmetry. The splitting of the $e_g$ and $e_u$ orbitals is expected to be small due to the similar magnitude of the $\pi$ and pseudo-$\sigma$ repulsive interactions. The $b_{2g}$ and $b_{1u}$ symmetry combinations of the $d_{xy}$ orbitals will undergo a moderate splitting since the $b_{1u}$ has a $\pi$ interaction with the acetate $a_2$ while the $b_{2g}$ remains nonbonding. One would therefore qualitatively predict that $J_{x^2-y^2,x^2-y^2}$ should have the largest antiferromagnetic contribution followed by $J_{xy,xy}$ and $J_{xzyz,xzyz}$ with $J_{z^2,z^2}$ having the smallest value. However, the values of $J_{n,n}$ estimated from experimental splittings (Table IV) indicate that $J_{xzyz,xzyz}$ has the largest antiferromagnetic value. It should be noted that while $J_{x^2-y^2,x^2-y^2}$ is an accurate experimental value, all other values of $J_{n,n}$ are subject to the approximations in eq 12 relating $J_{n,n}$ to $L_{n,x^2-y^2}$. However, $L_{xzyz,x^2-y^2}$ is experimentally much larger than $L_{xy,x^2-y^2}$, indicating that $J_{xzyz,xzyz}$ must be greater than $J_{xy,xy}$. Again, variation in the ferromagnetic contribution to $J_{n,n}$ can have significant effects. On the basis of arguments similar to those outlined for $J_{n,x^2-y^2}$, the ferromagnetic contribution to $J_{x^2-y^2,x^2-y^2}$ and $J_{xy,xy}$ should be large due to significant spin density in the $a_1$ and $a_2$ acetate orbitals, respectively. Additionally, the ferromagnetic contribution to $J_{xzyz,xzyz}$ will be smaller, because delocalization into both the $a_1$ and $b_2$ acetate orbitals will lower the overlap density in each region. Thus, the magnitude of $J_{x^2-y^2,x^2-y^2}$ and $J_{xy,xy}$ will be modified by large ferromagnetic terms, while $J_{xzyz,xzyz}$ should have a much smaller reduction. However, it must also be emphasized that a recent high level ab initio perturbative CI calculation of the origin of $J_{x^2-y^2,x^2-y^2}$ in copper acetate has found that in addition to the simple antiferromagnetic (kinetic) and ferromagnetic (potential) terms discussed above double-spin polarization and higher order terms contribute to the value of $J_{x^2-y^2,x^2-y^2}$ and are comparable in magnitude to the kinetic and potential terms.[19] Comparable calculations on these excited states would be required to obtain further quantitative insight into the values of $J$ for the different d orbital pathways considered in this study.

Many binuclear copper systems have an intense absorption band at approximately twice the energy of the ligand field features, which correlates with formation of the dimeric structure. This dimer band has previously been assigned as either a simultaneous pair excitation (SPE) or as a low-energy ligand-to-metal charge-transfer transition.[12,13] The dimer band in copper acetate pyrazine is observed in the absorption and MCD at 26 000 $cm^{-1}$, as shown in Figure 5. The clean $z$ molecular polarization of the absorption feature indicates that there is only one transition contributing in the dimer band region. The temperature dependence of the dimer band absorption intensity correlates with the population of the singlet component of the ground state, indicating that this is a singlet-to-singlet excitation. The fact that no MCD intensity is observed with increasing temperature demonstrates that a triplet component is not present and must be at least 4000 $cm^{-1}$ above the singlet. Similar behavior has recently been observed in the $Cu_2Cl_6^{2-}$ system where the dimer band was clearly assigned as the singlet component of a ligand-to-metal charge-transfer transition.[14] The large stabilization of this charge-transfer singlet, compared to that of the corresponding triplet, was associated with a large antiferromagnetic exchange coupling in the charge-transfer excited state relative to the ground state. By analogy, we assign the dimer band in copper acetate pyrazine as a $z$ polarized $^1A_{1g} \rightarrow {}^1A_{2u}$ ligand-to-metal charge-transfer transition. This transition can arise from a transfer of an electron from either the $a_1(b_{1g})$ or $b_2(b_{2u})$ orbital on the acetate bridge to the $d_{x^2-y^2}$ orbital on the copper. Although the $a_1$ orbital should be at deeper binding energy, it has good overlap with the $d_{x^2-y^2}$ leading to a large excited-state antiferromagnetic interaction, which will stabilize the singlet component of the charge-transfer excited state as is experimentally observed.

While attention in copper dimers has generally focused on ground-state magnetic properties, this study clearly emphasizes that the excited states also exhibit significant spectral effects due

(39) Although the $d_{xz,yz}$ orbitals span the A′ and A″ representations, no spectral splitting of these states is observed, indicating that no significant mixing with the $d_{x^2-y^2}$ orbital occurs due to the low symmetry distortion.

to dimer interactions. Furthermore, these excited-state interactions provide experimental insight into the superexchange pathways involving different combinations of d orbitals and, in addition, directly relate to the origin of the ground-state spin Hamiltonian parameters.

**Acknowledgment.** We thank Professor D. S. McClure for informing us of the excited-state vibronic structure exhibited by this system, Professor R. L. Musselman for information on crystal morphology, and Dr. J. J. Girerd for useful discussions. This research is supported by NIH Grant DK31450.

**Registry No.** Copper acetate pyrazine, 51798-90-4.

**Supplementary Material Available:** Spin-orbit matrixes for the even and odd parity dimer-state wave functions given in Table IB,C (2 pages). Ordering information is given on any current masthead page.

# Complexation of Tin(II) by the Iridium Metallomacrocycle $Ir_2(CO)_2Cl_2(\mu\text{-}Ph_2PCH_2As(Ph)CH_2PPh_2)_2$. A Novel Receptor and Sensor of Tin(II)

**Alan L. Balch,* Marilyn M. Olmstead, Douglas E. Oram, Philip E. Reedy, Jr., and Steven H. Reimer**

*Contribution from the Department of Chemistry, University of California, Davis, California 95616.* *Received July 25, 1988*

**Abstract:** Tin(II) chloride reacts with yellow $Ir_2(CO)_2Cl_2(\mu\text{-dpma})_2$ (dpma is $Ph_2PCH_2As(Ph)CH_2PPh_2$) to yield blue $[Ir_2(SnCl)(CO)_2Cl_2(\mu\text{-dpma})_2]SnCl_3$. The X-ray crystal structure of a derivative, $[Ir_2(SnCl)(CO)_2Cl_2(\mu\text{-dpma})_2][Ir(SnCl_3)_2(CO)(dpma)]$, which crystallizes in the triclinic space group $P\bar{1}$ with $a$ = 16.739 (7) Å, $b$ = 17.030 (7) Å, $c$ = 21.785 (9) Å, $\alpha$ = 79.61 (3)°, $\beta$ = 75.97 (3)°, $\gamma$ = 67.78 (3)°, $Z$ = 2 at 130 K, has been determined. Least-squares refinement of 665 parameters using 7363 reflections yielded $R$ = 0.063. The cation consists of the intact metallomacrocycle with the tin symmetrically bound only to the two iridium ions and a chloride (Ir-Sn distances, 2.741 (2) Å, 2.742 (2) Å, Sn-Cl, 2.443 (7) Å, Ir-Sn-Ir angle, 146.1°) in a planar arrangement. The anion consists of an iridium in a trigonal bipyramidal environment with a CO and P as the axial ligands. The dpma acts as a six-membered chelating ligand with the arsenic atom uncoordinated. $[Ir_2(SnCl)(CO)_2Cl_2(\mu\text{-dpma})_2]^+$ has an intense blue color, $\lambda_{max}$ = 588 ($\epsilon$ = 77000) and luminescence at 645 nm, that makes it a sensitive sensor for tin(II). $Ir_2(CO)_2Cl_2(\mu\text{-dpma})_2$ is capable of selectively extracting tin(II) from an aqueous solution containing Sn(II) and other metal ions and also is capable of transporting Sn(II) from one aqueous phase through dichloromethane to a second aqueous phase. The bonding in the IrSnIr chain is discussed in the context of other nearly linear trinuclear complexes.

The metallomacrocycle $Ir_2(CO)_2Cl_2(\mu\text{-dpma})_2$, **1** (dpma is bis(diphenylphosphinomethyl)phenylarsine), is capable of binding

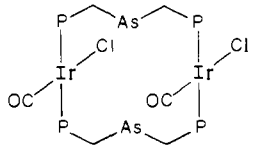

**1**

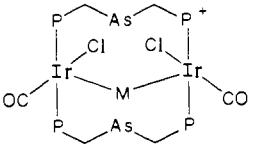

**2a**, M = Tl
**b**, M = Pb(NO$_3$)

a variety of heavy transition-metal ions through the formation of bonds to the arsenic, iridium, chloride, and/or carbon monoxide parts of **1**.[1] Examples of complexes with transition-metal ions, palladium(II),[2] rhodium(I),[3] iridium(I),[3] copper(I),[4] silver(I),[4,5] gold(III), and gold(I),[6,7] incorporated into **1** have been prepared and structurally characterized by X-ray crystallography.

Recently, we have discovered that **1** is also capable of binding main group ions with an $s^2$ electronic configuration. A communication describing the intensely colored, luminescent thallium(I) and lead(II) complexes **2** has been published.[8] In these novel materials, the thallium(I) and lead(II) ions are bound only by the two iridium ions of **1**; no bonds to chloride or arsenic are present. This is particularly remarkable since, as we point out in ref 8, the lower oxidation states of these metals, thallium(I) and lead(II), have only been infrequently found to engage in bonding to transition-metal ions.

Here we describe the interactions of **1** with another $s^2$ ion, tin(II). The interactions of tin(II) chloride with transition metals are well known.[9] Generally, with platinum metal halide complexes, insertion into M-Cl bonds can be anticipated with the formation of M-$SnCl_3$ units as the outcome. That is not the case with **1**.

## Results

**Synthesis and Characterization of the Complexes.** The first of the series of iridium-tin complexes was prepared by treating a dichloromethane solution of $Ir_2(CO)_2Cl_2(\mu\text{-dpma})_2$, **1**, with an excess of $SnCl_2\cdot 2H_2O$ in methanol. The initially yellow solution

(1) Balch, A. L. *Pure Appl. Chem.* **1988**, *60*, 555.
(2) Balch, A. L.; Fossett, L. A.; Olmstead, M. M.; Oram, D. E.; Reedy, P. E., Jr. *J. Am. Chem. Soc.* **1985**, *107*, 5272.
(3) Balch, A. L.; Fossett, L. A.; Olmstead, M. M.; Reedy, P. E., Jr. *Organometallics* **1986**, *5*, 1929.
(4) Balch, A. L.; Olmstead, M. M.; Neve, F.; Ghedini, M. *New J. Chem.* **1988**, *12*, 529.
(5) Balch, A. L.; Ghedini, M.; Oram, D. E.; Reedy, P. E., Jr. *Inorg. Chem.* **1987**, *26*, 1223.
(6) Balch, A. L.; Oram, D. E.; Reedy, P. E., Jr. *Inorg. Chem.* **1987**, *26*, 1836.
(7) Balch, A. L.; Nagle, J. K.; Oram, D. E.; Reedy, P. E., Jr. *J. Am. Chem. Soc.* **1988**, *110*, 454.
(8) Balch, A. L.; Nagle, J. K.; Olmstead, M. M.; Reedy, P. E., Jr. *J. Am. Chem. Soc.* **1987**, *109*, 4123.
(9) Young, J. F.; Gillard, R. D.; Wilkinson, G. *J. Chem. Soc.* **1964**, 5176. Anderson, G. K.; Clark, H. C.; Davies, J. A. *Inorg. Chem.* **1983**, *22*, 427, 434. Young, J. F. *Adv. Inorg. Chem. Radiochem.* **1968**, *11*, 91. Zubieta, J. A.; Zuckerman, J. J. *Prog. Inorg. Chem.* **1978**, *24*, 251. Olmstead, M. M.; Benner, L. S.; Hope, H.; Balch, A. L. *Inorg. Chim. Acta* **1979**, *32*, 193.

0002-7863/89/1511-4021$01.50/0 